Dear Mr. Montanher,

Many thanks for your valuable comments. Following your thoughtful and helpful suggestions, we have revised the manuscript carefully. The list below is the response.

General comments
Writing: Although my English is not very good, I've noted some writing errors along the paper. Although I've marked a few points, I strongly suggest an additional professional overhaul.
Response:

Thanks for correction of our manuscript in language and grammar. Following your suggestions, we have also asked for two associated professors of USA helping us to pick up writing errors and revise our manuscript very carefully. All the revising have been marked in red in the marked-up mode (Page 1, lines 1-2; Page 2, line 6; Page 3, lines 1-4, 26; Page 5, lines 7, 11, 20, 25; Page 6, lines 8, 16; Page 12, line 21; Page 15, lines 3, 14, 21; Page 16, line 13).

About the title: The title does not represents precisely the content of the paper. I think that it needs to include the geographic specificity of the model ("only" in China). This specification does not denigrate the research relevance, because the coastal environments of China are giant, have great social importance and have a rich remote sensing TSS modelling background.
Response:

Dear Mr. Montanher, following your suggestion, we added the geographic specification into the title (Page 1, lines 15, 19-20). We agree that the title "A Landsat-based model for retrieving total suspended solids concentration of estuaries and coasts in China" represents the content of the paper more precisely than the one before.

Page 1 (abstract): The abstract contains a great number of details concerning the validation and modelling results. However, a first read (without reading the whole paper) does not provided an understanding of the general strategy of modelling. For example, in the line 15 is written N=129, while in lines 18-20 the N (model) is 84 and N (validation) is 35 (84+35 = 119?). After this, another model is mentioned (lines 27-28). A reorganization of the abstract is needed, taking into account the explanation of the modelling, not only the specific indexes as RMSE and R^2.
Response:

We did the revision that there are **129** in total in-situ samples were collected from the study areas (Page 6, line 23). Among them, there are **119** in-situ samples with field spectral measurements and synchronous water samples (TSS concentration) (Page 7, lines 3-4. Table 1). **Another ten** in-situ samples have TSS concentration **only** while EO-1 Hyperion overpasses (Page 7, lines 4-5. Table 1). So, the **84 and 35** in-situ samples were used to calibrate and validate the

QRLTSS model respectively. Another **ten** in-situ samples of TSS were **only** used to validate the accuracy of the QRLTSS model **for remote sensing inversion of Hyperion image**. The line 27-28 mentioned was the threshold method of solving the two-valued issue of QRLTSS model.

A very important source of error in estimating water components concentration and/or water quality parameters is the sun glint effect. However, there are simple strategies to remove the glint which are based on the SWIR bands. These bands are available for many Landsat sensors. I suggest reading the following papers:
HEDLEY, J. D.; HARBORNE, A. R.; MUMBY, P. J. Simple and robust removal of sun glint for mapping shallow-water benthos. International Journal of Remote Sensing, v. 26, p. 2107-2112, 2005.
HOCHBERG, E. J.; ANDREFOUET, S.; TYLER, M. R. Sea surface correction of high spatial resolution IKONOS images to improve bottom mapping in near-shore environments. IEEE Transactions on Geoscience and Remote Sensing, v. 41, p. 1724 – 1729, 2003.
KAY, S.; HEDLEY, J. D.; LAVENDER, S. Sun Glint Correction of High and Low Spatial Resolution Images of Aquatic Scenes: a Review of Methods for Visible and Near-Infrared Wavelengths. Remote Sensing, v. 1, n. 4, p. 697-730, 2009.
Wang, M., 2007. Remote sensing of the ocean contributions from ultraviolet to near infrared using the shortwave infrared bands: simulations. Applied Optics 46, 1535–1547.
Wang, J.J., Lu, X.X., Liew, S.C., Zhou, Y., 2009. Retrieval of suspended sediment concentrations in large turbid rivers using Landsat ETM+: an example from the Yangtze River, China. Earth Surface Processes and Landforms 34, 1082–1092.

Following these references, I've used the band 5 (Landsat 5, TM) as a proxy of the Sun glint effect in modelling TSS in the Amazon basin (with co-authors, of course):
Montanher, O. C.; Novo, E. M. L. M.; Barbosa, C. C. F.; Renno, C. D.; Silva, T. S. F. Empirical models for estimating the suspended sediment concentration in Amazonian white water rivers using Landsat/TM. International Journal of Applied Earth Observation and Geoinformation, v. 29, p. 67-77, 2014.

Removing Sun glint effect might improve significantly your results. For example, even the reflectance threshold (0.032 in the red band,) could be affected by Sun glint, resulting in wrong choices (see equation 5 and page 12, lines 23-27). At this stage, performing the sun glint removal means remake all the work… So, this option could be a future strategy for your work.
Response:

Yes, the sun glint effect is indeed an important source of error in estimating water components concentration. However, the 6S atmospheric correction model this study used also corrects the skylight reflection (Sun and sky glint) following the Snell-Fresnel laws, environmental effects and directional target effects (Doxarana et al. 2002), and the Fresnel reflection is partially reduced by the presence of land in estuarial and coastal waters (Vidot and

Santer 2005). Actually, we **also agree** that there are still partial residues of glint effect remained. As we all know, each of atmospheric correction methods has its advantages and disadvantages. It is an interesting question and deserves our further study according to your suggestion. We have made partial revision in section 2.3 (Atmospheric correction method) for the clarity (Page 8, lines 9-12). The following references have been added.

Doxaran, D., Froidefond, J.M., Lavender, S., & Castaing, P.: Spectral signature of highly turbid waters Application with SPOT data to quantify suspended particulate matter concentrations. Remote Sensing of Environment, 81, 149-161, doi.org/10.1016/S0034-4257(01)00341-8, 2002.

HEDLEY, J.D., HARBORNE, A.R., MUMBY, P.J.: Simple and robust removal of sun glint for mapping shallow-water benthos. International Journal of Remote Sensing, 26(10), 2107-2112, DOI: 10.1080/01431160500034086, 2005.

Hochberg, E.J., Andréfouët, S., Tyler, M.R.: Sea surface correction of high spatial resolution IKONOS images to improve bottom mapping in near-shore environments. IEEE Transactions on Geoscience and Remote Sensing, 41(7), 1724-1729, DOI: 10.1109/TGRS.2003.815408, 2003.

Montanher, O.C., Novo, E.M.L.M., Barbosa, C.C.F., Renno, C.D., Silva, T.S.F.: Empirical models for estimating the suspended sediment concentration in Amazonian white water rivers using Landsat/TM. International Journal of Applied Earth Observation and Geoinformation, 29, 67-77, DOI: 10.1016/j.jag.2014.01.001, 2014.

Vidot, J., & Santer, R.: Atmospheric correction for inland waters-application to SeaWiFS. International Journal of Remote Sensing, 26, 3663-3682, DOI: 10.1080/01431160500034029, 2005.

Specific comments Page 1 - line 21: is there a statistical significant difference between the R^2 values? I think that the R^2 values difference does not justify: "The QRLTSS model based on Landsat OLI is better than TM and ETM+ ... because of the optimization of OLI sensor's design." A way to verify that may be by means of a statistical test. Page 9 – lines 9-16: This part of the manuscript is a methodology step, including the equation 3. Page 17 – line 13: this sentence is excessively repetitive along the whole paper: "a quadratic model using the ratio of logarithmic transformation of red band and near infrared band and logarithmic transformation of TSS concentration (QRLTSS) for estimating TSS concentration". If the acronym was proposed, would be better use it along the paper. Page 18 – line 7: the 30 m resolution only began in 1982, with Landsat4. Rewrite to take into account the 80 m MSS.

Response:

In fact, the difference between the R^2 values (calibration accuracy) of QRLTSS models based on OLI, ETM+ and TM is very small with the statistical significances (P-value < 0.001). The validation accuracy of QRLTSS models based on OLI is also a little better than ETM+ and TM (RMSE: 21.5 mg/L vs 25 mg/L and 24.9 mg/L, MRE: 27.2% vs 32.5% and 31.5%). We come to the conclusion of OLI better based on the integrated consideration of calibration and validation accuracy of the model, and the performance of different sensors. We have revised the corresponding statement to make it more clear (Page 1, lines 20-22).

The contents of the Part "Band response function application of Landsat sensors for field spectra" had been moved to Section 2.5 (Pages 9-10).

We have checked the manuscript and used the acronym (QRLTSS) along the paper to represent *"a quadratic model using the ratio of logarithmic transformation of red band and near infrared band and logarithmic transformation of TSS concentration for estimating TSS concentration"* (Page 17, lines 17 and 21).

On the beginning of 30 m resolution, we have modified the corresponding sentence as "Landsat imageries could be one of the best choices in terms of the availability of data source for remote sensing of TSS in estuaries and coasts, considering the spatial resolution and acquirement of long time series (30m TM/ETM+/OLI beginning in 1982, 80m MSS since 1972)" (Page 18, lines 2-3).

Technical corrections Page 4 - line 26: Based "on" the above analysis...Page 4 – line 28: Rewrite the beginning of the sentence: "And we focus on..." Figure 1: The map of China should be improved and noted as "a". Add a scale, coordinates, etc. Page 5 –lines 13-14: ton/year (or tons per year.), on average. $3\cdot10^4$ instead of using $3*10^4$. Reorganize these notations along the whole paper. Page 5 – line 21: 199 km and 6.103 km^2 Page 6 – lines 22-26: suggestion: include this information in a table. Page 7: "TM, ETM+ and OLI sensors onboard the Landsat 5, 7 and 8 satellites, respectively, have..."

Response:

We have revised the statements (Page 4, line 26) that you pointed out and checked the whole manuscript carefully (Page 4, line 24). The sentence "And we focus on the models examination of multiple bands combination, which belong to non-monotonic function" have been modified as "We focus on the models of multiple bands combination, and the form of models belongs to non-monotonic function." (Page 4, lines 26-27).

Following your suggestions, the associated hydrologic features (length, drainage area, mean surface runoff and sediment discharge) of five estuaries or coasts have been added into Table 1 (Page 25). The map of China was noted as "a", and added a scale, a north arrow, coordinates as well (Page 29). The revised Table 1 and Figure 1 have also been shown as follows

Once again, thank you very much for your valuable comments and suggestions.

The revised Table 1. Information about the study areas and in-situ data

Location	Hydrologic features (length, drainage area, mean surface runoff and sediment discharge)	Date	Samples	Measurements	Number of synchronous samples with satellite
Region I	$-$, $-$ $8.6\cdot10^8 m^3$/year, $3\cdot10^4$ ton/year	Dec 3, 2010	10	Reflectance, TSS	No
		Jan 13~14, 2013	22	Reflectance, TSS	No
Region II	199 km, $6\cdot10^3$ km^2, $8.21\cdot10^9$ m^3/year, $3.27\cdot10^5$ ton/year	Dec 6, 2013	11	Reflectance, TSS	7, OLI
Region III	2320 km, $4.53\cdot10^5$ km^2, $3.26\cdot10^{11}$ m^3/year, $7.53\cdot10^7$ ton/year	Dec 19, 2006	5	Reflectance, TSS	No
		Dec 21, 2006	18	8 samples with Reflectance and TSS; 10 samples with TSS only	13, Hyperion
		Dec 27, 2007	8	Reflectance, TSS	No
		Nov 2, 2012	9	Reflectance, TSS	6, ETM+
Region IV	470 km, $3.01\cdot10^4$ km^2, $2.45\cdot10^{10}$ m^3/year, $6.93\cdot10^6$ ton/year	Dec 1, 2013	12	Reflectance, TSS	9, OLI
Region V	6280 km, $1.8\cdot10^6$ km^2, $9.2\cdot10^{11}$ m^3/year, $4.8\cdot10^8$ ton/year	Oct 14~15, 2009	34	Reflectance, TSS	No

The revised Figure 1. Study areas and locations of in situ data. b: Xuwen coast; c: Moyangjiang River Estuary; d: Pearl River Estuary; e: Hanjiang River Estuary; f: Yangtze River Estuary.

A Landsat-based model for retrieving total suspended solids concentration of estuaries and coasts in China

Chongyang Wang[1,2,3], Shuisen Chen[2], Dan Li[2], Wei Liu[1,2,3], Ji Yang[1,2,3], Danni Wang[4]

[1] Guangzhou Institute of Geochemistry, Chinese Academy of Sciences, Guangzhou 510640, China

5　　[2] Guangzhou Institute of Geography, Guangzhou 510070, China

[3] University of Chinese Academy of Sciences, Beijing 100049, China

[4] Department of Resources and the Urban Planning, Xin Hua College of Sun Yat-Sen University, Guangzhou 510520, China

Correspondence to: Shuisen Chen (css@gdas.ac.cn)

10　　**Abstract.** Retrieving total suspended solids (TSS) concentration accurately is essential for sustainable management of estuaries and coasts, which plays a key role in the interaction of hydrosphere, pedosphere and atmosphere. Although many TSS retrieval models have been published, the general inversion method that is applicable to different field conditions is still under research. In order to obtain a TSS remote sensing model that is suitable for estimating the TSS concentrations with wide range in estuaries and coasts by Landsat imageries, this study recalibrated and validated a

15　　number of regression-techniques-based TSS retrieval models using 119 in-situ samples collected from five regions of China during the period of 2006-2013. It was found that the adjusted Quadratic model using the Ratio of Logarithmic transformation of red band and near infrared band and logarithmic transformation of TSS concentration (QRLTSS) works well and shows a relatively satisfactory performance. The adjusted QRLTSS model based on Landsat TM, ETM+ and OLI sensors explained about 72% of the TSS concentration variation (TSS: 4.3-577.2 mg/L, N=84. P-value

20　　< 0.001) and had an acceptable validation accuracy (TSS: 4.5-474 mg/L, RMSE: about 23 mg/L, N=35). The accuracy of QRLTSS model based on Landsat OLI is a little higher than TM and ETM+ due to the optimization of OLI sensor's design. A threshold method of red band reflectance (OLI: 0.032, ETM+ and TM: 0.031) was proposed to solve the two-valued issue of QRLTSS model and to retrieve TSS concentration from Landsat imageries. After 6S model-based atmospheric correction of Landsat OLI and ETM+ imageries, the TSS concentrations of three regions (Moyangjiang

25　　River Estuary, Pearl River Estuary and Hanjiang River Estuary) in Guangdong Province of China were mapped by the adjusted QRLTSS model. It was found that the TSS concentrations in the three estuaries showed large variation ranging from 0.295 mg/L to 370.4 mg/L. As a result, the Landsat imageries inversed TSS concentrations showed good validation accuracies with the synchronous in-situ observation (TSS: 7-160 mg/L, RMSE: 11.06 mg/L, N=22). The

1

further validation from EO-1 Hyperion imagery also showed good performance (in site synchronous measurement of TSS: 106-220.7 mg/L, RMSE: 26.66 mg/L, N=13) of the adjusted QRLTSS model for the area of high TSS concentrations in Lingding Bay of Pearl River Estuaries. Evidently, the adjusted QRLTSS model can be potentially applied to simulate high-dynamic TSS concentrations of other estuaries and coasts in the world by Landsat imageries, improving the understanding of the spatial and temporal variation of TSS concentrations on regional and global scales. We believe that the adjusted QRLTSS model can be further optimized to establish a regional or unified TSS retrieval model of estuaries and coasts for different satellite sensors similar to Landsat OLI-ETM+-TM sensors or with similar red and near infrared bands, such as ALI, HJ-1 A/B, LISS, CBERS, ASTER, ALOS, RapidEye, Kanopus-V, GF, etc.

Keywords: total suspended solids, estuaries and coasts, QRLTSS model, evaluation and optimization, remote sensing

1 Introduction

Total suspended solids (TSS) is a critical factor of the ecological environment of water bodies, which directly and deeply affects their optical properties through absorbing and scattering of the sunlight (Chen et al., 2015b; Pozdnyakov et al., 2005; Wang et al., 2016; Wu et al., 2013), leading to impacts on the primary production of the water areas (May et al., 2003). Estuaries and coasts are the most important intermediate zones that connect hydrosphere, pedosphere and atmosphere, which then pass on a deep and wide impact on many aspects of our societal and natural environment (Nechad et al., 2010; Pozdnyakov et al., 2005). The topic of TSS concentration monitoring and spatial and temporal variation assessment has been paid great attention, and the associated research work has been conducted frequently by a variety of scholars, government branches and society communities (Caballero et al., 2014; Giardino et al., 2015; Liu et al., 2003; Lu et al., 2012; Montanher et al., 2014; Nechad et al., 2010; Olmanson et al., 2013; Pozdnyakov et al., 2005; Rao et al., 2009; Shen et al., 2008; Tang et al., 2004b; Zhang et al., 2007). Many methods can be used to estimate TSS concentrations of water bodies, including hydrological sites monitoring, in-situ investigation, physical models, numerical simulation, remote sensing and so on (Chen et al., 2015a). Retrieving TSS concentrations from remote sensing data has unique advantages due to the wide spatial coverage and periodic revisit, such as Land Observation Satellite (Landsat), the first Earth Observing (EO-1), the Moderate Resolution Imaging Spectroradiometer (MODIS), the Medium Resolution Imaging Spectrometer (MERIS), the Geostationary Ocean Color Imager (GOCI), the Sea Viewing Wide Field of View Sensor (SeaWiFS), Systeme Probatoire d'Observation dela Tarre (SPOT) and the

Environment and Disaster Monitoring and Forecasting Small Satellite Constellation (HJ). Compared to other remote sensing data, Landsat series of imageries have advantage on spatiotemporal dynamics analysis of TSS concentrations (Wu et al., 2013) due to the additional good quality, high spatial resolution and inheritance, especially long-term historical data since 1972.

5

Many Landsat-based models have estimated the TSS concentration with empirical, semi-empirical, semi-analytical or analytical algorithms (Chen et al., 2014; Doxaran et al., 2003; Fraser., 1998; Islam et al., 2001; Li et al., 2010; Montanher et al., 2014; Nas et al., 2010; Oyama et al., 2009; Raharimahefa and Kusky., 2010; Rao et al., 2009; Ritchie and Cooper., 1991; Topliss et al., 1990; Volpe et al., 2011; Wang et al., 2016; Wu et al., 2013; Zhang et al., 2014).

10 Based on the rigorous theoretical derivation, the semi-analytical and analytical models are likely more applicable to different water bodies than the empirical or semi-empirical methods (Binding et al., 2012; Binding et al., 2010; Chen et al., 2015b; Giardino et al., 2007; Ma et al., 2010; Sipelgas et al., 2009). However, there are still limitations of the application due to the difficulties of retrieval or inaccuracies on initialization parameters (Binding et al., 2012; Chen et al., 2015b; Ma et al., 2010; Wu et al., 2013). Therefore, the empirical, especially semi-empirical methods are still used

15 to estimate TSS concentration, and will continue to be used for a long time due to their simplicity and sufficient accuracies. It should be noted that the applications of empirical or semi-empirical TSS models need to be revalidated in different regions and periods because they are largely region-, time- or environment dependent (Wu et al., 2013). We found that previous empirical or semi-empirical Landsat-based TSS retrieval models vary greatly in their forms (Ma et al., 2010; Wu et al., 2013).

20

The TSS models of single band include linear function (Fraser., 1998; Islam et al., 2001; Nas et al., 2010; Rao et al., 2009), exponential or logarithmic function (Keiner and Yan., 1998; Wu et al., 2013; Zhang et al., 2014) and quadratic function (Chen et al., 2014). Those models have been applied to many regions easily because they not only have the simple forms but also more choice of remote sensing data. We know that the sensitivity of satellite sensor bands is

25 different for different TSS concentrations. Many studies have proven that reflectance in the red band increases with the increasing of TSS concentrations but tends to convergence or keeps stable due to saturation effect of high TSS concentrations (Ritchie and Zimba., 2005; Feng et al., 2014), while the reflectance in the near infrared band is sensitive to high TSS concentrations although not sensitive for low TSS concentrations (Chen et al., 2015b; Feng et al., 2014; Hu et al., 2004; Wang et al., 2010). Thus, those models of single band have limited applications in regions with wide

3

dynamic TSS concentration range.

Models of multiple bands combination work better than a single band in avoiding the effect of saturation for water bodies of high TSS concentrations, and have been applied widely (Dekkera et al., 2001; Doxaran et al., 2003; Feng et al., 2014; Montanher et al., 2014; Oyama et al., 2009; Wang et al., 2016). Although the bands combination includes band ratio (Doxaran et al., 2003; Lathrop et al., 1991; Ritchie and Cooper., 1991; Topliss et al., 1990; Wang et al., 2016) and other complex forms (Dekkera et al., 2001; Li et al., 2010; Oyama et al., 2009; Song et al., 2011; Zhang et al., 2015), these models of multiple bands combination can be also classified into linear, exponential, logarithmic or quadratic function. Besides quadratic forms of models (Chen et al., 2014; Ritchie and Cooper., 1991; Topliss et al., 1990), most of those empirical or semi-empirical TSS retrieval models are simple monotonic functions. Monotonic function has some potential issues. One is that the change of band reflectance corresponds to the fixed change of TSS concentrations, which may be unrealistic, such as linear function. Another is that a little change of band reflectance can cause exaggerated estimation of TSS concentrations, such as exponential and logarithmic function. Although some non-monotonic functions could avoid the potential issues, it is widely believed that there does not exist a regional or universal empirical or semi- empirical TSS retrieval model for all water bodies (Ma et al., 2009; Tang et al., 2005; Wu et al., 2013).

Recently, we published a conference paper (Wang et al., 2016), which stated that the quadratic TSS model could be a new method for estimating TSS concentrations of multiple estuaries and coasts. However, the model lacks necessary analysis and discussion of results due to limitation of space. Also, our previous model (Wang et al., 2016) could not be applied to remote sensing data for the reason that each value of reflectance does not correspond to a unique TSS concentration.

Based on the above analysis, this study intends to further evaluate and validate the Landsat-based model for retrieving TSS concentrations in estuaries and coasts, and improve our previous work (Wang et al., 2016). To achieve this goal, the applicability of more than 20 previous Landsat-based models was reviewed and further analyzed. We focus on the models of multiple bands combination, and the form of models belongs to non-monotonic function. The issue of the model (Wang et al., 2016) that could not be applied to remote sensing data was solved by providing the TSS concentration division of vertex value of quatratic function. This paper was organized as follows. In-situ data,

pre-processing and Landsat imageries were described along with the atmospheric correction method and assessment method of simulation model accuracy in Section 2. The TSS retrieval model, validation and the spatial analysis of TSS concentration mapped from Landsat imageries and EO-1 Hyperion imagery were presented in Section 3. Finally, the summary and conclusions were given in Section 4.

2 Materials and methods

2.1 Study areas

The study areas including five regions of China are listed as follows.

Region I, Xuwen coast (Fig.1b), located between longitudes 109.8°~110.1°E and latitudes 20.1°~20.5°N, is the important Coral Reefs National Nature Reserve with the most plentiful coral species because of its less turbid waters. The good water quality is due to less water discharge ($8.6 \cdot 10^8 m^3$/year on average) and sediment load ($3 \cdot 10^4$ ton/year on average) (Wang et al., 2002). It was reported that the coral reefs does not grow as well as before (Zhao et al., 2011). Researchers believe that this is mainly caused by the increasing TSS concentration, declination of water transparency, and decreasing water temperature due to excessive fish farming, overfishing and industrial pollution (Chen et al., 2015b). The coastal land development is also an important reason.

Region II, Moyangjiang River Estuary (Fig.1c), is located between longitudes 112°~112.2°E and latitudes 21.65°~21.9°N, southwest of Guangdong Province. The source of Moyangjiang River is in Yangchun County, and it has a length of 199 km and a drainage area of more than $6 \cdot 10^3$ km². The annual mean surface runoff of Moyangjiang River is $8.21 \cdot 10^9 m^3$ and sediment load is $3.27 \cdot 10^5$ ton/year on average. Moyangjiang River crosses Yangchun, Yangdong and Jiangcheng Counties (Districts) and flows into the South China Sea.

Region III, Pearl River Estuary (Fig.1d), is located between longitudes 113.15°~114.1°E and latitudes 21.9°~23°N. Pearl River is the fourth longest (2320 km) in China with a drainage area of $4.53 \cdot 10^5$ km², and its annual runoff ($3.26 \cdot 10^{11} m^3$) is only smaller than Yangtze River. The sediment load of Pearl River is $7.53 \cdot 10^7$ ton/year on average. Pearl River crosses eight water ways, (Humen, Jiaomen, Hongqimen, Hengmen, Modaomen, Jitimen, Hutiaomen and

Yamen) located at six cities of Guangdong Province and pours into South China Sea. As we all know estuary and coast of Pearl River suffers severely from combined pollution (Ma and Wang 2003) which mainly comes from industrial production, residential life and seawater intrusion (Chen et al., 2009a).

5 Region IV, Hanjiang River Estuary (Fig.1e), is located between longitudes 116.6 °~117 °E and latitudes 23.2 °~23.6 °N, east of Guangdong Province and southwest of Fujian Province. Hanjiang River has a length of 470 km and has the second largest drainage area ($3.01 \cdot 10^4$ km^2) in Guangdong Province. The annual mean surface runoff of Hanjiang River is $2.45 \cdot 10^{10}$ m^3 with sediment load is $6.93 \cdot 10^6$ ton/year on average. The lower reaches of Hanjiang River include Beixi water way located in northeast, Dongxi water way located in the middle and Xixi water way located in the west.

10 Xixi water way also crosses with the three water ways of Waishahe, Xinjinhe and Meixi, and flows into the South China Sea. Waishahe, Xinjinhe and Meixi water ways are located in east, middle and west of Longhu District, Shantou of Gungdong Province, respectively.

Region V, Yangtze River Estuary (Fig.1f), is located between longitudes 121.55 °~122.4 °E and latitudes 30.8 °~31.8 °N.

15 Yangtze River is the largest river in China, and has a length of 6280 km and a drainage area of $1.8 \cdot 10^6$ km^2. The annual mean surface runoff of Yangtze River is $9.2 \cdot 10^{11}$ m^3 with sediment load is $4.8 \cdot 10^8$ ton/year on average (Feng et al., 2014). Such huge terrestrial input not only loads to its extremely turbid waters but also impacts on the optical properties of this region. It is reported that the environment of Yangtze River estuary is getting worse due to the rapid developments and urbanization in the surrounding industrial areas (Chen et al., 2015a; Hsu and Lin., 2010). As a result,

20 there are more and more studies focusing on this region due to its important ecological and economic role (Chen et al., 2015a; Feng et al., 2014; Shen et al., 2010).

2.2 In-situ and satellite data

The 129 in-situ samples were collected from the above-mentioned five regions of China, and their positions were recorded by Trimble global positioning system with root mean square errors of 1~4 m (shown in Fig.1). We used these

25 samples to establish the spectral model of TSS retrieval for estuaries and coasts. Among them, 32 samples were collected from Xuwen coast on December 3, 2010 and February 13~14, 2013; 11 samples were collected from Moyangjiang River Estuary on December 6, 2013; 40 samples were collected from Pearl River Estuary on December

19, 21, 2006, December 27, 2007 and November 2, 2012; 12 samples were collected from Hanjiang River Estuary on December 1, 2013; 34 samples were collected from Yangtze River Estuary on October 14~15, 2009. The field spectral measurements and synchronous water samples of the above-mentioned 119 samples were carried out from 10:00 to 15:00 (Fig.1, dots. Table 1). Besides, another ten samples with TSS only from Pearl River Estuary on December 21, 2006 were collected synchronous with Earth-observing (EO-1) Hyperion imagery (Fig.1d, triangles. Table 1). The spectrum were measured based on above-water spectrum measurement method (Tang et al., 2004a) which was applied to the water bodies like estuaries and coasts of China widely. Finally, the reflectance of water surface (Fig.2) were calculated in the same way as Zhang et al. (2014) and Chen et al. (2015b) did while TSS concentrations were measured from water samples by a weighed method (Binding et al., 2012; Caballero et al., 2014).

TM, ETM+ and OLI sensors onboard the Landsat 5, 7 and 8 satellites, respectively, have a spatial resolution of about 30m, with more than seven band spanning from visible to infrared wavelength. Landsat imagery can be fit for quantifying the optical properties in oceans, lakes, estuaries and coasts which have been explored in many studies although they were originally designed for observation of land targets (Zhang et al., 2014).

Due to frequent cloud coverage in estuaries and coasts, as well as the low temporal resolution (16d) of Landsat satellite (Bailey and Werdell., 2006), this study only obtained three Landsat imageries with good quality that can be matched with synchronous in-situ measurements of three study regions (Table 1). The first scene of image from ETM+ (path/row = 122/45) was captured on November 2, 2012, covering part of Pearl River Estuary (Fig.1d). The second scene of image (path/row = 120/44) from OLI was captured on December 1, 2013, covering Hanjiang River Estuary (Fig.1e). The third scene of image (path/row = 123/45) from OLI was captured on December 6, 2013, covering Moyangjiang River Estuary (Fig.1c). It should be noted that the scan line corrector (SLC) of Landsat 7 ETM+ has failed since May 31, 2003. However, there are still many research works using the SLC-off data that is repaired using local self-adaptive regression analysis (Zhang et al., 2014). The repaired data in our study is provided by the International Scientific Data service Platform, Computer Network Information Center, Chinese Academy of Sciences (http://datamirror.csdb.cn).

In addition, a scene of EO-1 Hyperion image (path/row=122/44) was captured on December 21, 2006, covering part of Pearl River Estuary (Fig.1d). With spectral coverage ranging from 400 to 2500 nm and 10 nm (sampling interval) of

7

contiguous bands of the solar reflected spectrum, Hyperion's spatial resolution is 30 m with a 7.7 km imagery swath and 185 km length (http://eo1.usgs.gov). Hyperion is also well suited for retrieving spatial distributions of water-color constituents in Pearl River Estuary (Chen et al., 2009a). The Hyperion data was used just for further validation of TSS retrieval model here.

2.3 Atmospheric correction method

Atmospheric correction is a necessary step before the remote sensing inversion (Gordon and Wang., 1994). The commonly used methods of atmospheric correction include the simple Dark Object Subtraction (DOS), Fast Line-of-sight Atmospheric Analysis of Spectral Hypercubes (FLAASH), and Second Simulation of Satellite Signal in the Solar Spectrum (6S) models. In addition, the regression analysis of spectral bands is also a common method used for atmospheric correction (Chen et al., 2011a; Mei et al., 2001; Montanher et al., 2014), which could remove the sun glint effect. Various research work (Doxarana et al., 2002; HEDLEY et al., 2003; Hochberg et al., 2003; Montanher et al., 2014; Vidot and Santer., 2005) have presented different atmospheric correction methods on the sun glint effect.

The 6S code the study used is the improved version of Simulation the Satellite Signal in the Solar Spectrum (5S), developed by the Laboratoire d'Optique Atmospherique (Vermote et al., 1997). It was frequently used for atmospheric correction of Landsat sensors based on the Landsat Ecosystem Disturbance Adaptive Processing System (LEDAPS, a Landsat atmospheric correction codebase funded by NASA's Terrestrial Ecology Program) (Feng et al., 2013; Ju et al., 2012; Maiersperger et al., 2013; Masek et al., 2006). The LEDAPS software was chosen for atmospheric correction in this paper. We assumed the continental aerosol type because the northeast monsoon was blowing from the land in the study. The aerosol optical thickness was derived independently from each Landsat acquisition using the dark dense vegetation (DDV) approach (Kaufman and Tanré, 1996). Critical atmospheric parameters of 6S model, including water vapor at a resolution of 2.5 by 2.5 degrees (http://dss.ucar.edu/datasets/ds090.0/) and ozone concentrations at a resolution of 1.25 longitude and 1 latitude, were collected from National Centers for Environmental Prediction (NCEP) and Total Ozone Mapping Spectrometer (TOMS) or NOAA's Television Infrared Observation Satellite Program (TIROS) Operational Vertical Sounder (TOVS), respectively (Feng et al., 2013; Ju et al., 2012; Masek et al., 2006). Rayleigh scattering was adjusted to local conditions by a static 0.05 degree digital topography dataset (derived from the 1 km GTopo30) and NCEP surface pressure data (Feng et al., 2013; Masek et al., 2006). All the parameters are

automatically called corresponding to each Landsat image when LEDAPS runs. The global surface reflectance products from Landsat of high quality had been obtained using LEDAPS implementation of 6S model (Feng et al., 2013; Maiersperger et al., 2013).

2.4 Accuracy assessment method of models

In order to validate the accuracy of the TSS retrieval models, atmospheric correction and mapping of TSS concentrations, the determination coefficient (R^2), the root mean square error (RMSE) and mean relative error (MRE) were calculated using the following equations, respectively.

$$RMSE = \sqrt{\frac{\sum\limits_{i=1}^{i=n}\left(x_i - x_i^{'}\right)^2}{n}} \qquad (1)$$

$$MRE = \frac{\sum\limits_{i=1}^{i=n}\left|\dfrac{x_i - x_i^{'}}{x_i}\right|}{n} \times 100\% \qquad (2)$$

Where x_i is the observed value, $x_i^{'}$ is the modeled value, i is the i th element, and n is the number of elements.

2.5 Band response function application of Landsat sensors for field spectra

Before establishing TSS retrieval model, the water surface reflectance measured in the field were convoluted with the Landsat band response functions to derive the band-weighted reflectance data using equation (3). It is also a critical step for the application of TSS retrieval model from ground spectral data to remote sensing imageries.

$$R(\text{band}) = \frac{\sum\limits_{band_{min}}^{band_{max}} f(\lambda_{band})r(\lambda_{band})}{\sum\limits_{band_{min}}^{band_{max}} f(\lambda_{band})} \qquad (3)$$

Where $band_{min}$ and $band_{max}$ are the lower and upper limits of Landsat band in red and near infrared bands, respectively. $r(\lambda)$ is the water surface reflectance; $f(\lambda)$ is the spectral response function of Landsat sensors (http://Landsat.usgs.gov).

9

Two simulated "R(band)", corresponding to the two Landsat bands (red band and near infrared band), were calculated for each samples.

3 Results and discussions

3.1 Review of previous Landsat-based TSS models

The previous Landsat-based TSS retrieval models (Table 2) were calibrated and validated again with the adjustment of parameters based on the 119 in-situ samples (84 in-situ samples for calibration, the other 35 for validation), shown in Fig.3. The results indicated that the previous Landsat-based TSS models did not explain the TSS variation so well when they were used to estuaries and coasts in the study. The determination coefficient of calibration models in the five best TSS models (Fig.3) is between 0.58 and 0.784, corresponding to linear (Fig.3c1) and quadratic (Fig.3a1) model of single band, respectively.

Based on the other 35 in-situ samples with range of 4.5-474 mg/L, we further validated the five TSS retrieval models. The results showed that minimum MRE is 39.4% from exponential model of single band (Fig.3d2) but its RMSE is 50.26 mg/L. The quadratic model of single band (Fig.3a2) got minimum RMSE (35.73 mg/L) but with high MRE value of 144.2%. Obviously, the quadratic model of single band is hard to be adopted for this study. However, for the exponential model of single band, its high RMSE prevents this form of model from its application as well, especially when we take the TSS concentration of 22 validation data lower than 36 mg/L (Fig.3 triangles) into account. The RMSEs and MREs of the other three forms of models are 69.3 mg/L and 45%, 82.7 mg/L and 48% for linear model (Fig.3b2 and c2), 68.7 mg/L and 41.3% for quadratic model (Fig.3e2), respectively. In contrast, the non-monotonic function, quadratic model of ratio of bands (Fig.3e) has a better performance among the five previous TSS models. But, we still expect that there would be a TSS model with high calibration and validation accuracy for estuaries and coasts of China by Landsat imageries simultaneously.

3.2 Development of QRLTSS model

In order to develop a Landsat-based model with higher calibration and validation accuracy, some MODIS-based TSS

retrieval models (Chen et al., 2009b; Chen et al., 2011ab; Chen et al., 2015b; Wang et al., 2010) were referred. These models made full use of the relationship between the ratio of logarithmic transformation of red band and near infrared band and logarithmic transformation of TSS concentration. Thus, following the feature of these MODIS based models, we further adjusted the model (Fig.3e1) that developed by Ritchie and Cooper. (1991), under MATLAB environment, shown in Fig.4.

From Fig.3 and Fig.4 (a1, b1 and c1), we found that the quadratic model of the ratio of logarithmic transformation of red band and near infrared band and logarithmic transformation of TSS concentration (QRLTSS, equation (4)) has a higher calibration accuracy than most of the previous TSS models, no matter whether it is Landsat OLI, ETM+ or TM sensor.

$$\frac{Log(R_1)}{Log(R_2)} = a*(Log(TSS))^2 + b*Log(TSS) + c \qquad (4)$$

Where R_1 and R_2 represent near infrared band and red band of OLI, ETM+ and TM sensors. Parameters a, b and c refer to Fig.4, respectively. The unit of TSS concentration is in mg/L.

Compared to the previous model developed by Ritchie and Cooper. (1991), we improved the input with logarithmic transformation of bands and made full use of the different sensitivity of red and near infrared bands to TSS concentrations that have been proved by many studies (Chen et al., 2015b; Feng et al., 2014; Wang et al., 2010; Hu et al., 2004). Compared to the MODIS-based models developed by Chen et al. (2011b) and Wang et al. (2010), the QRLTSS model established in this paper seems more complicated. The models (Chen et al., 2011b; Wang et al., 2010) are in linear or exponential form, belonging to simple monotonic function that can cause unreliable estimation in some spectral range. Although the QRLTSS model developed in our study is similar to previous studies (Chen et al., 2009b; Chen et al., 2011a; Chen et al., 2015b), there are some differences among them. They are indeed all quadratic models, but the models developed by Chen et al. (2009b) and Chen et al. (2011a) are part of the curve. It is different from the form developed by Chen et al. (2015b) and this study, which are all complete quadratic curve. It should be noted that the part of quadratic model has limitation in estimating TSS concentration with the wide range. Some regions with lower or higher TSS concentration could not be retrieved accurately. In fact, TSS concentrations in the study area (Apalachicola Bay, USA) of Chen et al. (2009b) and Chen et al. (2011a) are not as high as TSS concentrations in study areas of this paper and Chen et al. (2015b). The maximum TSS concentration in the previous studies was about 200

11

mg/L (Chen et al., 2009b; Chen et al., 2011a), but the maximum TSS concentration was more than 500 mg/L (Yangtze River Estuary) for previous study (Chen et al., 2015b) and this study. In addition, the study areas of Chen et al. (2015b) only include Xuwen Coral Reef National Nature Reserve, a less turbid region, and Yangtze River Estuary, an extremely turbid region, which might make the model developed by Chen et al. (2015b) perform worse in the middle of the quadratic curve than both ends of the quadratic curve. The QRLTSS model in this study is better in the continuity of calibration and validation data than Chen et al. (2015b). The reason is that the study areas of this paper include not only their regions (Chen et al., 2015b) but also other three main estuarine regions, Guangdong province (Moyangjiang River Estuary, Pearl River Estuary and Hanjiang River Estuary). In general, the TSS concentrations in the three additional regions are higher than Xuwen coast, but lower than Yangtze River Estuary. These data are good supplement for the robustness of an accurate model on the previous study.

It should be noted that a band value corresponds to two TSS concentrations values based on the QRLTSS model (equation (4)). We should make the unique choice when validating or retrieving TSS concentration by the model. Unfortunately, we had not been aware of this problem and did not solve it in our previous work (Wang et al., 2016). It meant that our previous results (Wang et al., 2016) were not complete. In this study, the TSS concentrations of vertex corresponding to the three quadratic models based on Landsat OLI, ETM+ and TM sensors have been obtained through solving the equations (Fig.4a1, b1 and c1). The vertex values are about 36.1 mg/L for OLI and about 32.2mg/L for ETM+ and TM, which attribute to their almost same spectral band features (Table 4). For QRLTSS model based on OLI sensor, we found that the values of OLI red band weighted reflectance of all validation data are lower than 0.032 when TSS concentrations are less than 36.1 mg/L (Fig.5a, blue dots) except for one exceptional data (Fig.5a, black dot). The reflectance is higher than 0.032 when TSS concentrations are more than 36.1 mg/L (Fig.5a, red dots). The QRLTSS models based on ETM+ and TM sensor have similar situations. But the values of TSS concentration and reflectance at vertex are 32.2 mg/L and 0.031, shown in Fig.5b (dots for ETM+ and triangles for TM). The findings are different from the result found in MODIS-based model by Chen et al. (2015b). In previous study (Chen et al., 2015b), the values of TSS concentration and reflectance of MODIS red band at vertex are 31 mg/L and 0.025, respectively. We believe that the difference was caused by different spectral characteristics of satellite sensors (Table 4). This is also why multi-source satellite remote sensing becomes more and more important in recent years. Monitoring TSS concentrations from multiple data sources could make full use of the advantages of all kinds of satellite sensors. According to the above analysis, TSS concentration can be retrieved by using equation (5) in the form of positive

squared root if the reflectance of red band is lower than 0.032 (OLI sensor) or 0.031 (ETM+ and TM sensors), and using equation (5) in the form of negative squared root if the reflectance of red band is greater than 0.032 (OLI sensor) or 0.031 (ETM+ and TM sensors), respectively.

$$Log(TSS)=\frac{-b\pm\sqrt{b^2-4a\left(c-\dfrac{Log(R_1)}{Log(R_2)}\right)}}{2a}, \left(b^2-4a\left(c-\dfrac{Log(R_1)}{Log(R_2)}\right)\geq 0\right) \quad (5)$$

We validated the QRLTSS model based on the 35 in-situ samples and the selection criteria (equation (5)). The results indicated that the QRLTSS model has a better performance than the previous five TSS models although QRLTSS model explained about 72% of the TSS concentration variation only. The RMSEs and MREs of all validation data for QRLTSS model are 21.5 mg/L and 27.2% for OLI (Fig.4a2), 25 mg/L and 32.5% for ETM+ (Fig.4b2), and 24.9 mg/L and 31.5% for TM (Fig.4c2), respectively. All of the simulated results from QRLTSS model have higher validation accuracies than the best of the five previous TSS models (RMSE: 35.7 mg/L, MRE: 39.4%). According to the vertex location of the quadratic model, the wide range of validation data (TSS: 4.5-474 mg/L) was divided into two parts of low (4.5-32.2 mg/L, triangles in Fig.3 and Fig.4) and high (36.2-474 mg/L, squares in Fig.3 and Fig.4) TSS concentration for further validation. For the data of low TSS concentrations, the RMSEs and MREs of validation are 3.5 mg/L and 31.1% for OLI, 4.6 mg/L and 38.3% for ETM+, and 4 mg/L and 35.3% for TM. For the data of high TSS concentrations, the RMSEs and MREs of validation are 35.1 mg/L and 20.7% for OLI, 40.7 mg/L and 20.3% for ETM+, and 40.6 mg/L and 25.1% for TM. The validation accuracies of the two parts are still better than the best of the previous five TSS models (RMSEs & MREs: 5.6 mg/L & 39.4% for low concentration part, and 53.5 mg/L & 23.5% for high concentration part). The detailed information of calibration and validation in Fig.3 and Fig.4 were shown in Table 3.

From Table 3 we could also find that the calibration and validation accuracy of OLI-based QRLTSS model is a little higher than ETM+ and TM (R^2: 0.7181 vs 0.708 and 0.7079, RMSE: 21.5 mg/L vs 25 mg/L and 24.9 mg/L, MRE: 27.2% vs 32.5% and 31.5%). We attribute this mainly to the improvement of Landsat OLI sensor's design. Especially for OLI band_5, the band of water vapor absorption at 825 nm were removed from the near infrared band range, whose wavelength is 845-885 nm now (http://Landsat.usgs.gov/Landsat8.php). While the near infrared band wavelength of ETM+ is 775-900 nm, and 760-900 nm for TM. In addition, the red band wavelength of OLI is 630-680 nm, and

630-690 nm for ETM+ and TM. The little difference between ETM+ and TM sensors determines a little difference in QRLTSS model based on ETM+ and TM. The performance (red band and near infrared band) of different sensors and the vertexes of the QRLTSS model based on these sensors were shown in Table 4.

3.3 Comparison of Landsat measured reflectance with in-situ reflectance

In order to analyze the spatial and temporal variation of TSS concentrations in our study areas and further verify accuracy of QRLTSS model, the acquired Landsat imageries were used to calculate the TSS concentrations by the QRLTSS model described in Section 3.2 (Equation (5)). First of all, Landsat imageries should be well calibrated by atmospheric correction, which is critical for working with multi-scene imageries and using empirical/semi-empirical method. Then the atmospheric correction accuracy of 6S was calculated based on the reflectance of synchronous in-situ measurements, a total of 22 samples from three regions within two-hour time window of satellite overpass. Six of the total 22 samples were collected from Pearl River Estuary on November 2, 2012, nine samples were collected from Hanjiang River Estuary on December 1, 2013 and the other seven samples were collected from Moyangjiang River Estuary on December 6, 2013. In deriving the reflectance comparison, the water-leaving radiances from Landsat imageries were averaged by windows of 3x3 pixels. We then calculated RMSE and MRE of the reflectance result after atmospheric correction with in-situ reflectance. RMSEs and MREs of red and near infrared bands are 0.0033, 9.58% and 0.00092, 21.5%, respectively, which showed an acceptable accuracy. Fig.6 shows that the 6S model is sufficiently stable and accurate for deriving the reflectance at visible and near infrared band from broadband satellite data for the purpose of remote sensing applications in estuarine and coastal waters.

3.4 Validation of QRLTSS model from Landsat imageries

After atmospheric correction of 6S, the TSS concentrations of Moyangjiang River Estuary, part of Pearl River Estuary, Hanjiang River Estuary were estimated from ETM+ or OLI imageries (Fig.7). Water bodies were extracted based on method developed by Jiang et al (2014). The difference of spectral profile across water and cloud were used to mask clouds (Chen et al., 2009; Chen et al., 2011a). In estuary and coast of Pearl River, we find that the reflectance of water is usually less than 0.05 in near infrared band while the reflectance of cloud is usually more than 0.1 in near infrared band. Thus, the clouds were masked based on reflectance that is more than 0.05 in near infrared band.

In Fig.7a, the TSS concentrations in Moyangjiang River Estuary (Beijing time at 11:00), on December 6, 2013 showed a large variation ranging from 0.557 mg/L to 203.9 mg/L. It is clear that the TSS concentrations are higher inside and outside of Moyangjiang River Estuary than outer shelf area, especially in the estuary downstream, with a mean value of 154.2 mg/L (Fig.7a). The region of high TSS concentrations in Moyangjiang River Estuary looks lung-shaped. The outer shelf area has low TSS concentrations, where the TSS concentrations less than 35 mg/L were frequently found and the maximum is not more than 60 mg/L. So, there are sharp fronts that could be seen clearly between coastal area and outer shelf area. The TSS distribution in Moyangjiang River Estuary mainly attribute to interaction of tide and runoff. In this study, the remote sensing imagery covering Moyangjiang River Estuary was obtained at 11:00 in the morning when the tide had begun to ebb and runoff with large amounts of sediment flowing into the South China Sea.

Different from TSS concentrations in Moyangjiang River Estuary, the TSS concentrations in eastern Zhuhai & Macao and Hongkong coastal water bodies are much lower, with a mean value of 12 mg/L (Fig.7b. Blank areas without synchronous image). There is a significant decreasing trend of TSS concentration from the northwest to southeast of Pearl River Estuary. It is mainly due to the interaction between runoff (flowing towards southwest) and tide (flowing towards northwest). The maximum TSS concentration is about 29 mg/L. The reason why the water bodies in outer Lingding Bay of Pearl River Estuary have a low level TSS concentration is mainly because of strong management protection and less human activity. Most part of eastern Zhuhai water bodies belong to Pearl River Estuary Chinese White Dolphin National Nature Reserve (CWDNNR) since 2003 (http://www.gdofa.gov.cn/). The CWDNNR has about 460 km^2 located between longitudes 113.66°~113.87°E and latitudes 21.18°~22.4°N, shown in Fig.7b (region with black dotted line). The low TSS concentrations in this region confirms the protection effect of Chinese White Dolphin.

Compared to Moyangjiang River Estuary and eastern Zhuhai and Macao coastal water bodies, the TSS concentrations in Hanjiang River Estuary had wider variables, ranging from 0.295 mg/L to 370.4 mg/L. The water bodies with high TSS concentrations in this region were mainly in two zones where the sharp fronts were clearly visible (Fig.7c, 1 and 2). The TSS concentrations in zone 1 were almost more than 100 mg/L with maximum value of 370.4 mg/L and a mean value of 167.91 mg/L. For zone 2, the TSS concentrations mainly ranged from 20 mg/L to 110 mg/L, and the maximum and mean value were 127.14 mg/L and 61.57 mg/L. The results also showed that the turbid river runoff

15

flows into South China Sea along east coast of Dahao District, Shantou City. The high TSS concentrations in this region were caused by different factors. In zone 1 at opposite bank of Dahao District, Shantou, it was mainly caused by the runoff of Xixi waterway, Hanjiang River and flow guiding line (Dam, solid black line in Fig.1e and Fig.7c) connected to Longhu District, Shantou City. While in zone 2, the high TSS concentrations were resulted from the interaction of tide current and runoff, which is the potential location of estuarine barrier bar. The TSS concentrations in estuary of Xinjinhe waterway, Hanjiang River are less than 50 mg/L. Our findings are similar to the results of Ding and Xu. (2007), which showed TSS concentrations ranged from 0.1 mg/L to 300 mg/L in Hanjiang River Estuary.

We also validated the accuracy of TSS concentration estimated from Landsat imageries (two OLIs and one ETM+) with in-situ samples that were collected from Pearl River Estuary, Hanjiang River Estuary and Moyangjiang River Estuary. The validation accuracy was shown in Fig.7d. The RMSE and MRE of comparison between 22 field TSS concentrations (7-160 mg/L) and Landsat satellite inversion are 11.06 mg/L and 24.1%, respectively. This indicated that the QRLTSS model is applicable to the mapping of TSS in the three estuaries from Landsat imageries.

3.5 Further validation of QRLTSS model from EO-1 Hyperion imagery

We were fortunate to acquire a scene of EO-1 Hyperion imagery at 10:33 (Beijing time) with synchronous TSS samples (N=13, ten sites with symbol of triangles and three sites with symbol of dots, Fig.1d) on December 21, 2006 covering part of Pearl River Estuary from northeast to southwest of the Lingding Bay. The data set gives us an opportunity to further validate the accuracy of the QRLTSS model. After similar pre-processing steps with Landsat imageries, the EO-1 Hyperion imagery was also used to retrieve TSS concentrations using the QRLTSS model. The results of TSS concentration mapping and validation accuracy were shown in Fig.8.

The TSS concentration mapping from Hyperion image on December 21, 2006 ranged from 1.79 mg/L to 361.6 mg/L, with a mean value of 124.4 mg/L (Fig.8a). The mapping results of TSS showed large variation from northeast to southwest in Pearl River Estuary. The areas of low TSS concentration were detected near the southwest of Lingding Bay (mostly in CWDNNR, Fig.7b) and in deep channels (east channel and west channel, Fig.8a) of Lingding Bay. The areas of high TSS concentration were in accordance with the outlets of different waterways (Humen, Jiaomen, Hongqimen and Hengmen) of Pearl River Estuary frequently or the foreshores, which indicate that it is the maximum

turbidity zones of the estuary. The 13 synchronous samples (TSS: 106-220.7 mg/L) were mostly collected from the northern zone of high TSS concentrations (Fig.1d). Comparisons of accuracy validation between in-situ and Hyperion imagery inversed TSS concentrations were produced in Fig.8b. The RMSE and MRE of comparison are 26.66 mg/L and 12.6%, respectively. It showed that the QRLTSS model also worked well in area of high TSS concentrations from

5 Hyperion mapping result of Pearl River Estuary.

Based on the evaluation and analysis of all the above results (Fig. 3, 4, 7 and 8. Table 3 and 4), we conclude that QRLTSS model has the advantage for quantitative inversion of TSS concentrations with a high dynamic range in estuaries and coasts. These results explained the usability of QRLTSS model by the validation of multi-spectral

10 Landsat OLI/ETM+ and hyperspectral EO-1 Hyperion imageries compared to our previous work (Wang et al., 2016).

4 Summary and conclusions

This study evaluated and adjusted a QRLTSS model for estimating TSS concentration of estuaries and coasts from Landsat imageries. The adjusted QRLTSS model had reasonable accuracy for wide TSS concentration variables in estuaries and coasts. In addition, the adjusted QRLTSS model was further validated by the independent in-situ samples.

15 We found that the adjusted model had the best validation accuracy among the 25 examined TSS retrieval models (Table 2 and 3), for the whole (4.5-474 mg/L), low (4.5-32.2 mg/L) and high (36.2-474 mg/L) range of TSS concentrations. We also found that the QRLTSS model based on the bands of OLI showed a higher accuracy than bands of ETM+ and TM (Table 3 and Fig.4), which can be explained by the adjusted band design of OLI sensor in reducing the effect of water vapor absorption compared to ETM+ and TM sensors (Table 4).

20

The adjusted QRLTSS model showed good performance when applied to estimate TSS concentrations from Landsat OLI/ETM+ imageries (Fig.7). The RMSEs and MREs of validation accuracy in Moyangjiang River Estuary (December 6, 2013), part of Pearl River Estuary (November 2, 2012) and Hanjiang River Estuary (December 1, 2013) are 11.06 mg/L and 24.1% for the whole range (7-160 mg/L), 3.75 mg/L and 22% for the low range (7-28.2 mg/L), and

25 24.69 mg/L and 33.2% for the high range (37-160 mg/L) of TSS concentrations, respectively. In addition, the high validation accuracy of TSS mapping from Hyperion imagery of Pearl River estuary (December 21, 2006) with in-situ data (106-220.7 mg/L) using the QRLTSS model had also been obtained (Fig.8, RMSE: 26.66 mg/L, MRE: 12.6%).

17

Landsat imageries could be one of the best choices in terms of the availability of data source for remote sensing of TSS in estuaries and coasts, considering the spatial resolution and acquirement of long time series (30m TM/ETM+/OLI beginning in 1982, 80m MSS since 1972). The research shows that the adjusted QRLTSS model can quantify the TSS concentration variation of estuaries and coasts by Landsat series of imageries with applicable accuracies (R^2: 0.71-0.72, 30m), which can be compared to the accuracies of previous OLI/ETM+/TM based studies (R^2: 0.67-0.92, 30m (Chen et al., 2014; Nas et al., 2010)) and MODIS-based studies (R^2: 0.61-0.86, 250m (Chen et al., 2011a; Wang et al.,2010)). The TSS concentrations at vertex of QRLTSS model based on Landsat sensors are different from MODIS (Table 4). Based on the vertex of QRLTSS model, we proposed a threshold (corresponding to the vertex of quadratic function) of red band reflectance (Fig.5, OLI: 0.032, ETM+ and TM: 0.031) which can be used to divide the quadratic function for solving the improved QRLTSS model under two kinds of squared roots (Table 4).

For a lot of medium- and high- resolution remote sensing sensors similar to Landsat series satellites, such as HJ-1 A/B, LISS, CBERS, ASTER, ALOS, RapidEye, Kanopus-V, GF, etc, we deduce that there is potential to optimize the QRLTSS model for mapping the wide range TSS concentrations of estuaries and coasts. It will be beneficial to remote sensing communities if the QRLTSS model can be further calibrated and validated based on different remote sensing sensors corresponding to different water bodies. This will provide great help in establishing regional or unified TSS semi-empirical remote sensing model of estuaries and coasts in the world.

Code and data availability

The LEDAPS code used for atmospheric correction and all the remote sensing imageries are fully available in the supplement to the article.

Acknowledgments

like to thank USGS for providing the Landsat imagery. Thanks are also given to the International Scientific Data Service Platform, Computer Network Information Center, Chinese Academy of Sciences for providing gap filled ETM+ SLC-off data (http://datamirror.csdb.cn).

References

5   Bailey, S.W., & Werdell, P.J.: A multi-sensor approach for the on-orbit validation of ocean color satellite data products. Remote Sensing of Environment, 102, 12-23, doi.org/10.1016/j.rse.2006.01.015, 2006.

Binding, C.E., Greenberg, T.A., & Bukata, R.P.: An Analysis of MODIS-Derived Algal and Mineral Turbidity in Lake Erie. Journal of Great Lakes Research, 38, 107-116, doi.org/10.1016/j.jglr.2011.12.003, 2012.

Binding, C.E., Jerome, J.H., Bukata, R.P., & Booty, W.G.: Suspended particulate matter in Lake Erie derived from MODIS
10   aquatic colour imagery. International Journal of Remote Sensing, 31, 5239-5255, DOI: 10.1080/01431160903302973, 2010.

Caballero, I., Morris, E.P., Ruiz, J., & Navarro, G.: Assessment of suspended solids in the Guadalquivir estuary using new DEIMOS-1 medium spatial resolution imagery. Remote Sensing of Environment, 146, 148–158, doi.org/10.1016/j.rse.2013.08.047, 2014.

15   Chen, J., Quan, W., Cui, T., & Song, Q.: Estimation of total suspended matter concentration from MODIS data using a neural network model in the China eastern coastal zone. Estuarine, Coastal and Shelf Science, 155, 104-113, doi.org/10.1016/j.ecss.2015.01.018, 2015a.

Chen, S., Fang, L., Zhang, L., & Li, D.: Remote sensing of turbidity in seawater intrusion reaches of Pearl River estuary: A case study in Modaomen waterway of Pearl River estuary，China. Estuarine，Coastal and Shelf Science, 82, 119-127,
20   doi:10.1016/j.ecss.2009.01.003, 2009a.

Chen, S., Han, L., Chen, X., Li, D., Sun, L., & Li, Y.: Estimating wide range Total Suspended Solids concentrations from MODIS 250-m imageries: An improved method. ISPRS Journal of Photogrammetry and Remote Sensing, 99, 58–69, doi.org/10.1016/j.isprsjprs.2014.10.006, 2015b.

Chen, S., Huang, W., Wang, H., & Li, D.: Remote sensing assessment of sediment re-suspension during Hurricane Frances in
25   Apalachicola Bay, USA. Remote Sensing of Environment, 113, 2670–2681, doi:10.1016/j.rse.2009.08.005, 2009b.

Chen, S., Huang, W.R., Chen, W.Q., & Chen, X.Z.: An enhanced MODIS remote sensing model for detecting rainfall effects on sediment plume in the coastal waters of Apalachicola Bay. Marine Environmental Research, 72, 265–272,

doi:10.1016/j.marenvres.2011.09.014, 2011a.

Chen, S., Huang, W.R., Chen, W.Q., & Wang, H.Q.: Remote sensing analysis of rainstorm effects on sediment concentrations in Apalachicola Bay, USA. Ecological Informatics, 6, 147–155, doi:10.1016/j.ecoinf.2010.12.001, 2011b.

Chen, Y., Kong, J., Sun, X., Du, D., & Cheng, P.: Retrieval of sea surface suspended sediment concentration in Bohai Gulf Offshore area based on semi-analysis model. Geography and Geo-Information Science, 30, 33-36,55, doi:10.3969/j.issn.1672-0504.2014.03.008, 2014.

Dekkera, A.G., Vosb, R.J., & Petersb, S.W.M.: Comparison of remote sensing data, model results and in-situ data for total suspended matter žTSM/ in the southern Frisian lakes. The Science of the Total Environment, 268, 197-214, DOI: 10.1016/S0048-9697(00)00679-3, 2001.

Ding, X., & Xu, X.: A remote sensing analysis of characteristics of Suspended sediments movement in Hanjiang estuary. REMOTE SENSING FOR LAND & RESOURCES, 3, 71-74, doi:10.3969/j.issn.1001-070X.2007.03.016, 2007.

Doxaran, D., Froidefond, J.M., & Castaing, P.: Remote-sensing reflectance of turbid sediment-dominated waters. Reduction of sediment type variations and changing illumination conditions effects by use of reflectance ratios. Applied Optics, 42, 2623-2634, DOI: 10.1364/AO.42.002623, 2003.

Doxaran, D., Froidefond, J.M., Lavender, S., & Castaing, P.: Spectral signature of highly turbid waters Application with SPOT data to quantify suspended particulate matter concentrations. Remote Sensing of Environment, 81, 149-161, doi.org/10.1016/S0034-4257(01)00341-8, 2002.

Feng, L., Hu, C., Chen, X., & Song, Q.: Influence of the Three Gorges Dam on total suspended matters in the Yangtze Estuary and its adjacent coastal waters: Observations from MODIS. Remote Sensing of Environment, 140, 779–788, doi.org/10.1016/j.rse.2013.10.002, 2014.

Feng, M., Sexton, J.O., Huang, C., Masek, J.G., Vermote, E.F., Gao, F., Narasimhan, R., Channan, S., Wolfe, R.E., & Townshend, J.R.: Global surface reflectance products from Landsat: Assessment using coincident MODIS observations. Remote Sensing of Environment, 134, 276-293, 2013.

FRASER, R.N.: Multispectral remote sensing of turbidity among Nebraska Sand Hills lakes. International Journal of Remote Sensing, 19, 3011-3016, doi.org/10.1016/j.rse.2013.02.031, 1998.

Giardino, C., Brando, V.E., Dekker, A.G., Strömbeck, N., & Candiani, G.: Assessment of water quality in Lake Garda (Italy) using Hyperion. Remote Sensing of Environment, 109, 183–195, doi:10.1016/j.rse.2006.12.017, 2007.

Giardino, C., Bresciani, M., Valentini, E., Gasperini, L., Bolpagni, R., & Brando, V.E.: Airborne hyperspectral data to assess suspended particulate matter and aquatic vegetation in a shallow and turbid lake. Remote Sensing of Environment, 157,

48–57, doi.org/10.1016/j.rse.2014.04.034, 2015.

Gordon, H.R., & Wang, M.: Retrieval of water-leaving radiance and aerosol optical thickness over the oceans with SeaWiFS: a preliminary algorithm. Applied Optics, 33, 443-452, doi.org/10.1364/AO.33.000443, 1994.

HEDLEY, J.D., HARBORNE, A.R., MUMBY, P.J.: Simple and robust removal of sun glint for mapping shallow-water benthos. International Journal of Remote Sensing, 26(10), 2107-2112, DOI: 10.1080/01431160500034086, 2005.

Hochberg, E.J., Andréfouët, S., Tyler, M.R.: Sea surface correction of high spatial resolution IKONOS images to improve bottom mapping in near-shore environments. IEEE Transactions on Geoscience and Remote Sensing, 41(7), 1724-1729, DOI: 10.1109/TGRS.2003.815408, 2003.

Hsu, S.-C., & Lin, F.J.: Elemental characteristics of surface suspended particulates off the Changjiang estuary during the 1998 flood. Journal of Marine Systems, 81, 323–334, doi:10.1016/j.jmarsys.2010.03.001, 2010.

Hu, C., Chen, Z., Clayton, T.D., Swarzenski, P., Brock, J.C., & Muller-Karger, F.E.: Assessment of estuarine water-quality indicators using MODIS medium-resolution bands: Initial results from Tampa Bay, FL. Remote Sensing of Environment, 93, 423-441, DOI: 10.1016/j.rse.2004.08.007, 2004.

Huang, W., Mukherjee, D., & Chen, S.: Assessment of Hurricane Ivan Effects on Chlorophyll-a in Pensacola Bay by MODIS 250m Remote Sensing. Marine Pollution Bulletin, 62, 490-498, doi:10.1016/j.marpolbul.2010.12.010, 2011.

Islam, M.R., Yamaguchi, Y., & Ogawa, K.: Suspended sediment in the Ganges and Brahmaputra Rivers in Bangladesh: observation from TM and AVHRR data. HYDROLOGICAL PROCESSES, 15, 493–509, DOI: 10.1002/hyp.165, 2001.

Jiang, H., Feng, M., Zhu, Y., Lu, N., Huang, J., & Xiao, T.: An Automated Method for Extracting Rivers and Lakes from Landsat Imagery. Remote Sensing, 6, 5067-5089, doi: 10.3390/rs6065067, 2014.

Ju, J., Roy, D.P., Vermote, E., Masek, J., & Kovalskyy, V.: Continental-scale validation of MODIS-based and LEDAPS Landsat ETM+ atmospheric correction methods. Remote Sensing of Environment, 122, 175-184, doi:10.1016/j.rse.2011.12.025, 2012.

Kaufman, Y.J., & Tanré, D.: Strategy for direct and indirect methods for correcting the aerosol effect on remote sensing: From AVHRR to EOS–MODIS. Remote Sensing of Environment, 55, 65-79, doi:10.1016/0034-4257(95)00193-X, 1996.

Keiner, L.E., & Yan, X.H.: A Neural Network Model for Estimating Sea Surface Chlorophyll and Sediments from Thematic Mapper Imagery. Remote Sensing of Environment, 66, 153–165, doi.org/10.1016/S0034-4257(98)00054-6, 1998.

LATHROP, R.G., LILLESAND, T.M., & YANDELL, B.S.: Testing the utility of simple multi-date Thematic Mapper calibration algorithms for monitoring turbid inland waters. International Journal of Remote Sensing, 12(10), 2045-2063, doi.org/10.1080/01431169108955235, 1991.

Li, J., Shu, G., & Yaping, W.: Delineating suspended sediment concentration patterns in surface waters of the Changjiang Estuary by remote sensing analysis. Acta Oceanologica Sinica, 29, 38-47, DOI: 10.1007/s13131-010-0054-7, 2010.

Liu, Y., Islam, M.A., & Gao, J.: Quantification of shallow water quality parameters by means of remote sensing. Progress in Physical Geography, 27, 24-43, DOI: 10.1191/0309133303pp357ra, 2003.

5   Lu, C., Lv, H., & Li, Y.: Backscattering properties and parametric model of Taihu Lake based on spectral classification. Journal of Remote Sensing, 16, 417-434, 2012.

Ma, D., & Wang, J.: Evaluation on potential ecological risk of sediment pollution in main estuaries of China. China Environmental Science, 23, 521-525, 2003.

Ma, R., Duan, H., Tang, J., & Chen, Z.: Remote sensing of lake water environment. Beijing: Science Press, 2010.

10   Ma, R., Tang, J., Duan, H., & Pan, D.: Progress in lake water color remote sensing. Journal of Lake Sciences, 21, 143-158, DOI: 10.18307/2009.0201, 2009.

Maiersperger, T.K., Scaramuzza, P.L., Leigh, L., Shrestha, S., Gallo, K.P., Jenkerson, C.B., & Dwyer, J.L.: Characterizing LEDAPS surface reflectance products by comparisons with AERONET, field spectrometer, and MODIS data. Remote Sensing of Environment, 136, 1-13, doi.org/10.1016/j.rse.2013.04.007, 2013.

15   Masek, J.G., Vermote, E.F., Saleous, N.E., Wolfe, R., Hall, F.G., Huemmrich, K.F., Gao, F., Kutler, J., & Lim, T.-K.: A Landsat Surface Reflectance Dataset for North America, 1990–2000. IEEE GEOSCIENCE AND REMOTE SENSING LETTERS, 3, 68-72, doi:10.1109/LGRS.2005.857030, 2006.

May, C.L., Koseff, J.R., Lucas, L.V., Cloern, J.E., & Schoellhamer, D.H.: Effects of spatial and temporal variability of turbidity on phytoplankton blooms. MARINE ECOLOGY PROGRESS SERIES, 254, 111-128, DOI: 20   10.3354/meps254111, 2003.

Mei, A., Peng, W., Qin, Q., & Liu, H.: Introduction to Remote Sensing. Beijing: Higher Eduction Press, 2001.

Montanher, O.C., Novo, E.M.L.M., Barbosa, C.C.F., Renno, C.D., Silva, T.S.F.: Empirical models for estimating the suspended sediment concentration in Amazonian white water rivers using Landsat/TM. International Journal of Applied Earth Observation and Geoinformation, 29, 67-77, doi.org/10.1016/j.jag.2014.01.001, 2014.

25   Nas, B., Ekercin, S., Karabörk, H., Berktay, A., & Mulla, D.J.: An Application of Landsat-5TM Image Data for Water Quality Mapping in Lake Beysehir, Turkey. Water Air Soil Pollut, 212, 183-197, DOI: 10.1007/s11270-010-0331-2, 2010.

Nechad, B., Ruddick, K., & Park, Y.: Calibration and validation of a generic multisensor algorithm for mapping of total suspended matter in turbid waters. Remote Sensing of Environment, 114, 854–866, doi:10.1016/j.rse.2009.11.022, 2010.

Olmanson, L.G., Brezonik, P.L., & Bauer, M.E.: Airborne hyperspectral remote sensing to assess spatial distribution of water

quality characteristics in large rivers-The Mississippi River and its tributaries in Minnesota. Remote Sensing of Environment, 130, 254–265, doi.org/10.1016/j.rse.2012.11.023, 2013.

Oyama, Y., Matsushita, B., Fukushima, T., Matsushige, K., & Imai, A.: Application of spectral decomposition algorithm for mapping water quality in a turbid lake (Lake Kasumigaura, Japan) from Landsat TM data. ISPRS Journal of Photogrammetry and Remote Sensing, 64, 73-85, doi:10.1016/j.isprsjprs.2008.04.005, 2009.

Pozdnyakov, D., Shuchman, R., Korosov, A., & Hatt, C.: Operational algorithm for the retrieval of water quality in the Great Lakes. Remote Sensing of Environment, 97, 352-370, doi:10.1016/j.rse.2005.04.018, 2005.

Raharimahefa, T., & Kusky, T.M.: Environmental Monitoring of Bombetoka Bay and the Betsiboka Estuary, Madagascar, Using Multi-temporal Satellite Data. Journal of Earth Science, 21, 210-226, DOI: 10.1007/s12583-010-0019-y, 2010.

Rao, K.H.V.D., Singh, A.K., & Roy, P.S.: Study of Morphology and Suspended Sediment of Bhopal Upper Lake using Spatial Simulation Technique and Remote Sensing Data. Indian Society of Remote Sensing, 37, 433–441, DOI: 10.1007/s12524-009-0034-6, 2009.

Ritchie, J.C., & Cooper, C.M.: An algorithm for estimating surface suspended sediment concentrations with Landsat MSS digital data. WATER RESOURCES BULLETIN, 27, 373-379, DOI: 10.1111/j.1752-1688.1991.tb01436.x, 1991.

Ritchie, J. C., & Zimba, P. V.: In M. G. Anderson (Ed.), 62: Estimation of Suspended Sediment and Algae in Water Bodies, DOI: 10.1002/0470848944.hsa066, 2005.

Shen, F., SALAMA, M.S., ZHOU, Y.-X., LI, J.-F., SU, Z., & KUANG, D.-B.: Remote-sensing reflectance characteristics of highly turbid estuarine waters – a comparative experiment of the Yangtze River and the Yellow River. International Journal of Remote Sensing, 31, 2639–2654, DOI: 10.1080/01431160903085610, 2010.

Shen, Z., Zhou, S., & Pei, S.: Transfer and transport of phosphorus and silica in the turbidity maximum zone of the Changjiang estuary. Estuarine, Coastal and Shelf Science, 78, 481-492, doi:10.1016/j.ecss.2008.01.010, 2008.

Sipelgas, L., Ossipova, V., Raudsepp, U., & Lindfors, A.: A bio-optical model for the calculation of suspended matter concentration form MODIS data in Pakri Bay, the gulf of Finland. BOREAL ENVIRONMENT RESEARCH, 14, 415-426, 2009.

Song, K., Wang, Z., Blackwell, J., Zhang, B., Li, F., Zhang, Y., & Jiang, G.: Water quality monitoring using Landsat Themate Mapper data with empirical algorithms in Chagan Lake, China. Journal of Applied Remote Sensing, 5, 053506-053516, doi: 10.1117/1.3559497, 2011.

Tang, J., Tian, G., Wang, X., Wang, X., & Song, Q.: The Methods of Water Spectra Measurement and Analysis: Above-Water Method. Journal of Remote Sensing, 8, 37-44, 2004a.

Tang, J., Wang, X., Song, Q., Li, T., Chen, J., Huang, H., & Ren, J.: The statistic inversion algorithms of water constituents for the Huanghai Sea and the East China Sea. Acta Oceanologica Sinica, 23, 617-626, 2004b.

Tang, W., Ma, C., Niu, S., Wang, X., Song, Q., & Ding, J.: Quantitative inversion of the water body composition based on CBERS02 datas. Science China E Information Sciences, 35, 156-170, 2005.

5 Topliss, B.J., Almos, C.L., & Hill, P.R.: Algorithms for remote sensing of high concentration, inorganic suspended sediment. International Journal of Remote Sensing, 11, 947-966, doi.org/10.1080/01431169008955069, 1990.

Vermote, E.F., Tanré, D., Deuzé, J.L., Herman, M., & Morcrette, J.-J.: Second Simulation of the Satellite Signal in the Solar Spectrum, 6S: An Overview. IEEE TRANSACTIONS ON GEOSCIENCE AND REMOTE SENSING, 35, 675-686, DOI: 10.1109/36.581987, 1997.

10 Vidot, J., & Santer, R.: Atmospheric correction for inland waters-application to SeaWiFS. International Journal of Remote Sensing, 26, 3663-3682, DOI: 10.1080/01431160500034029, 2005.

Volpe, V., Silvestri, S., & Marani, M.: Remote sensing retrieval of suspended sediment concentration in shallow waters. Remote Sensing of Environment, 115, 44-54, DOI: 10.1016/j.rse.2010.07.013, 2011.

Wang, C., Li, D., Wang, D., Chen, S., & Liu, W.: A total suspended sediment retrieval model for multiple estuaries and coasts
15 by Landsat imageries. 2016 4th International Workshop on Earth Observation and Remote Sensing Applications, DOI: 10.1109/EORSA.2016.7552785, 2016.

Wang, H., Hladik, C.M., Huang, W., Milla, K., Edmiston, L., Harwell, M.A., & Schalles, J.F.: Detecting the spatial and temporal variability of chlorophylla concentration and total suspended solids in Apalachicola Bay, Florida using MODIS imagery. International Journal of Remote Sensing, 31, 439-453, DOI: 10.1080/01431160902893485, 2010.

20 Wang, L., Zhao, H., Song, C., Yuan, J., & Yu, H.: Coastal geomorphic evolut ion at the Denglou Cape, the Leizhou Peninsula. Acta Oceanologica Sinica, 21, 597-611, 2002.

Wu, G., Cui, L., Duan, H., Fei, T., & Liu, Y.: An approach for developing Landsat-5 TM-based retrieval models of suspended particulate matter concentration with the assistance of MODIS. ISPRS Journal of Photogrammetry and Remote Sensing, 85, 84–92, doi.org/10.1016/j.isprsjprs.2013.08.009, 2013.

25 Zhang, M., Dong, Q., Cui, T., Xue, C., & Zhang, S.: Suspended sediment monitoring and assessment for Yellow River estuary from Landsat TM and ETM+ imagery. Remote Sensing of Environment, 146, 136–147, doi.org/10.1016/j.rse.2013.09.033, 2014.

Zhang, Y., Zhang, B., Wang, X., Li, J., Feng, S., Zhao, Q., Liu, M., & Qin, B.: A study of absorption characteristics of chromophoric dissolved organic matter and particles in Lake Taihu, China. Hydrobiologia, 592, 105–120, DOI:

10.1007/s10750-007-0724-4, 2007.

Zhang, Y., Zhang, Y., Zha, Y., Shi, K., Zhou, Y., & Wang, M.: Remote Sensing Estimation of Total Suspended Matter Concentration in Xin'anjiang Reservoir Using Landsat 8 Data. Environmental Science, 36, 56-63, DOI: 10.13227/j.hjkx.2015.01.008, 2015.

5   Zhao, H., Chen, Q., Walker, N.D., Zheng, Q., & Macintyre, H.L.: A study of sediment transport in a shallow estuary using MODIS imagery and particle tracking simulation. International Journal of Remote Sensing, 32, 6653-6671, DOI: 10.1080/01431161.2010.512938, 2011.

Tables

10   **Table 1.** Information about the study areas and in-situ data

Location	Hydrologic features (Length, drainage area, mean surface runoff and sediment discharge)	Date	Samples	Measurements	Number of synchronous samples with satellite
Region I	$-$, $-$ $8.6 \cdot 10^8$ m^3/year, $3 \cdot 10^4$ ton/year	Dec 3, 2010	10	Reflectance, TSS	No
		Jan 13~14, 2013	22	Reflectance, TSS	No
Region II	199 km, $6 \cdot 10^3$ km^2, $8.21 \cdot 10^9$ m^3/year, $3.27 \cdot 10^5$ ton/year	Dec 6, 2013	11	Reflectance, TSS	7, OLI
Region III	2320 km, $4.53 \cdot 10^5$ km^2, $3.26 \cdot 10^{11}$ m^3/year, $7.53 \cdot 10^7$ ton/year	Dec 19, 2006	5	Reflectance, TSS	No
		Dec 21, 2006	18	8 samples with Reflectance and TSS; 10 samples with TSS only	13, Hyperion
		Dec 27, 2007	8	Reflectance, TSS	No
		Nov 2, 2012	9	Reflectance, TSS	6, ETM+
Region IV	470 km, $3.01 \cdot 10^4$ km^2, $2.45 \cdot 10^{10}$ m^3/year, $6.93 \cdot 10^6$ ton/year	Dec 1, 2013	12	Reflectance, TSS	9, OLI
Region V	6280 km, $1.8 \cdot 10^6$ km^2, $9.2 \cdot 10^{11}$ m^3/year, $4.8 \cdot 10^8$ ton/year	Oct 14~15, 2009	34	Reflectance, TSS	No

Table 2. Review of previous TSS or Turbidity retrieval models using Landsat imagery.

Data	Model	Study area	Reference
TM 2 and 4	TSS=29.022•exp(0.0335•(B4/B2))	Gironde and Loire Estuaries	Doxaran et al. (2003)
MSS 5 and 6	Ln(TSS)= 1.4•(B5/B6)^2-6.2•(B5/B6) +10.8	the Bay of Fundy and the Beaufort Sea	Topliss et al. (1990)
TM 1, 3, 4	Turbidity=11.31•(B4/B1)-2.03•B3-16.42	Chagan Lake	Song et al. (2011)
TM 1, 2, 3 or 4	Turbidity=16.1•B4-12.7 Turbidity=10•B3-24.8 Turbidity=19•B1-97.9 Turbidity=6.4•B2-28	Nebraska Sand Hills Lakes	Fraser. (1998)
TM 3	TSS=69.39•B3-201	Ganges and Brahmaputra Rivers	Islam et al. (2001)
MSS 1 and 2	Ln(TSS)= 2.71•(B1/B2)^2-9.21•(B1/B2) +8.45	Enid Reservoir in North Central Mississippi	Ritchie and Cooper. (1991)
TM 3	Log(TSS)= 0.098•B3+0.334	Delaware Bay	Keiner and Yan. (1998)
TM 2 and 3	TSS=0.7581•exp(61.683•(B2+B3)/2)	southern Frisian lakes	Dekkera et al. (2001)
TM 1 and 3	TSS=0.0167•exp(12.3•B3/B1)	an embayment of Lake Michigan	Lathrop et al. (1991)
TM 3 and ETM+ 3	Log(TSS)= 44.072•B3 +0.1591	Yellow River estuary	Zhang et al. (2014)
TM 3 and 4	TSS=2.19•exp(21.965•B3) TSS=-9275.78•(B3)^3+8623.19•(B3)^2 -810.04•B3+23.44	Poyang Lake	Wu et al. (2013)

	$TSS=5829.8 \cdot (B3-B4)^3+4165.09 \cdot (B3-B4)^2$ $-189.88 \cdot (B3-B4)+5.43$ $TSS=3.411 \cdot exp(21.998 \cdot (B3-B4))$		
OLI 2, 3 and 8	$TSS=-191.02 \cdot B2+36.8 \cdot B3+172.66 \cdot B8+4.57$	Xin'anjiang Reservoir	Zhang et al. (2015)
TM 2	$B2=0.0044 \cdot TSS+2.5226$	Bhopal Upper Lake	Rao et al. (2009)
TM 2 and 3	$Log(TSS)= 6.2244 \cdot (B2+B3)/B2 \cdot B3+0.892$	Yangtze estuary	Li et al. (2010)
TM 3	$TSS=0.543 \cdot B3-7.102$	Beysehir Lake	Nas et al. (2010)
TM 4	$TSS=229457.695 \cdot (B4)^2+146.462 \cdot B4+5.701$	Bohai gulf	Chen et al. (2014)

5

Table 3. The comparison of calibration and validation accuracy of several best TSS retrieval models

Model form		Calibration R^2	Validation (RMSE(mg/L), MRE)		
			Whole	Low range	High range
Chen et al. (2014)		0.7842	35.7, 144.2%	18.35, 215.58%	53.56, 23.5%
Li et al. (2010)		0.6167	69.3, 45%	5.66, 52.6%	113.48, 32.1%
Zhang et al. (2014)		0.5804	82.8, 48%	6.56, 53.9%	135.54, 38.15%
Lathrop et al. (1991)		0.6661	50.3 39.4%	6.12, 44.6%	82.09, 30.57%
Ritchie and Cooper. (1991)		0.6983	68.7, 41.3%	7.24, 44%	112.32, 36.6%
QRLTSS	OLI	0.7181	21.5, 27.2%	3.5, 31.1%	35.1, 20.7%
model	ETM+	0.708	25, 32.5%	4.6, 38.3%	40.7, 20.3%
based on	TM	0.7079	24.9, 31.5%	4, 35.3%	40.6, 25.1%

10

Table 4. The performance of different sensors and the vertexs of QRLTSS model based on these sensors

	TM	ETM+	OLI	MODIS
	Red band, Near infrared band	Red band, Near infrared band	Red band, Near infrared band	Red band, Near infrared band
Wavelength (nm)	630-690, 760-900	630-690, 775-900	630-680, 845-885	620-670, 841-874
Spatial resolution (m)	30	30	30	250
Radiometric resolution (bit)	8	8	12	12
Signal/noise (dB. Specified level of high)	140, 244	140, 244	340, 460	128, 201
The vertex of quadratic model	0.031, 32.2 mg/L (This study)	0.031, 32.2 mg/L (This study)	0.032, 36.1 mg/L (This study)	0.025, 31 mg/L (Chen et al., 2015b)

5

10

15

20

Figures
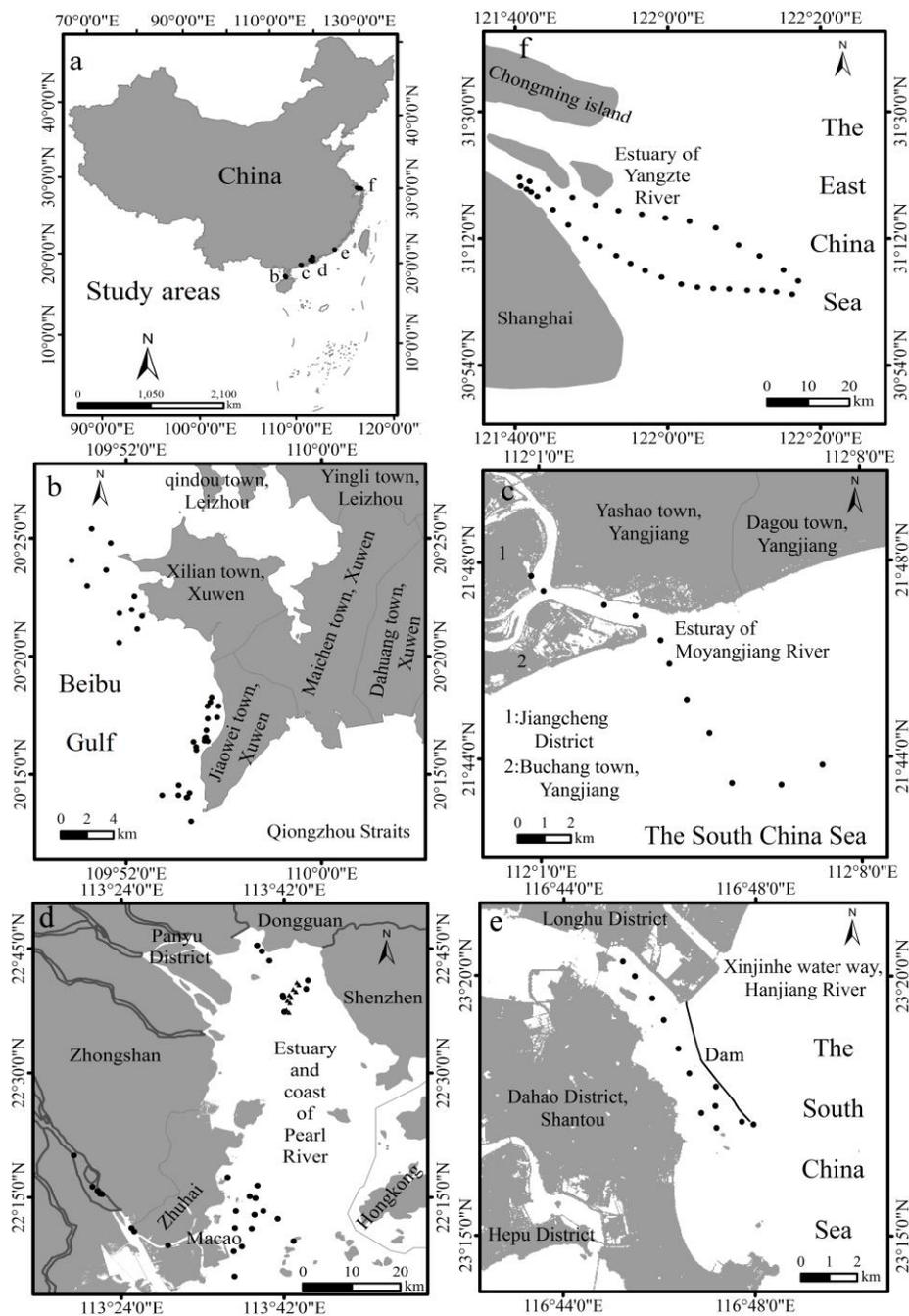
Figure 1. Study areas and locations of in situ data. b: Xuwen coast; c: Moyangjiang River Estuary; d: Pearl River Estuary; e: Hanjiang River Estuary; f: Yangtze River Estuary.

5
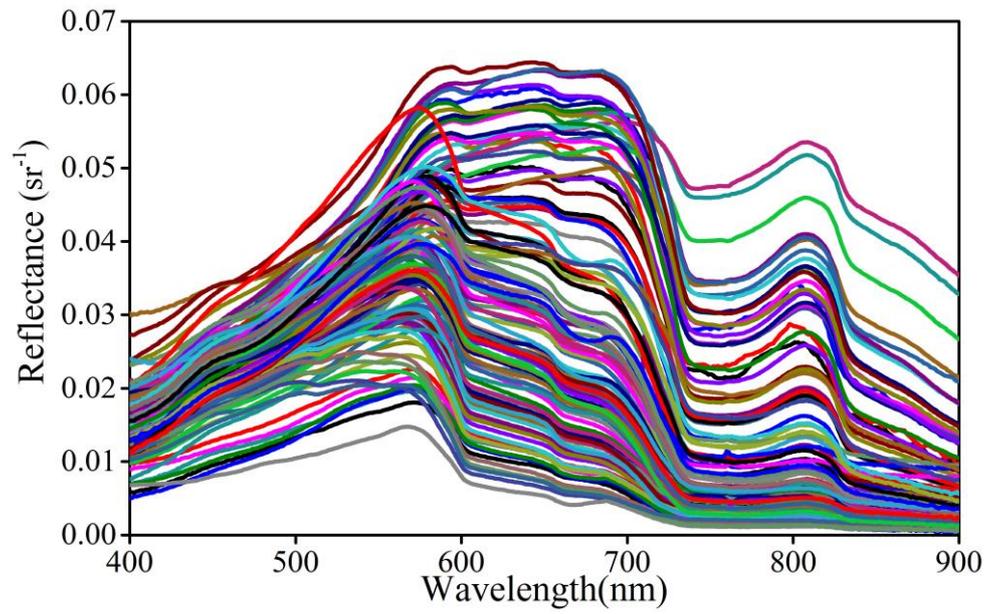
**Figure 2.** 119 spectra were collected from study areas by ASD
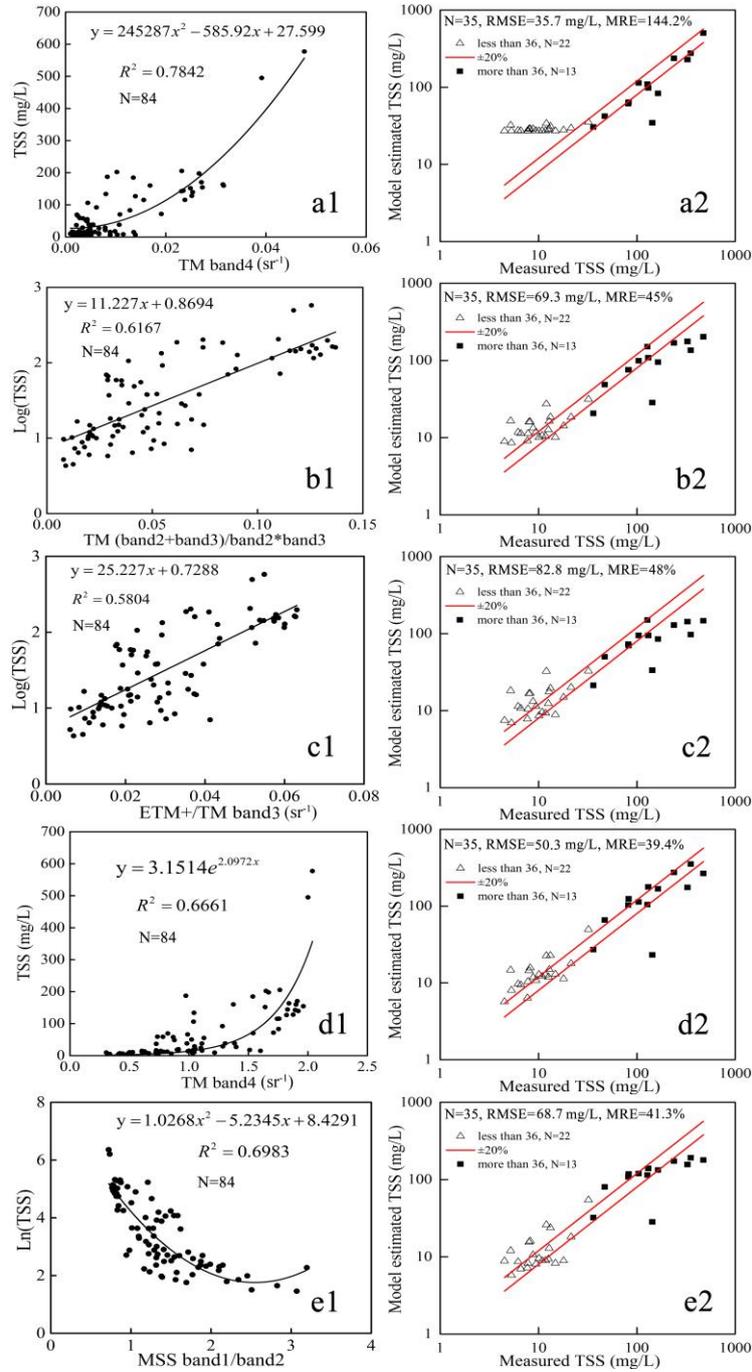
Figure 3. The recalibration and validation of previous five TSS retrieval models based on 119 in situ samples. The models were developed by a (Chen et al., 2014), b (Li et al., 2010), c (Zhang et al., 2014), d (Lathrop et al., 1991), e (Ritchie and Cooper., 1991), respectively.
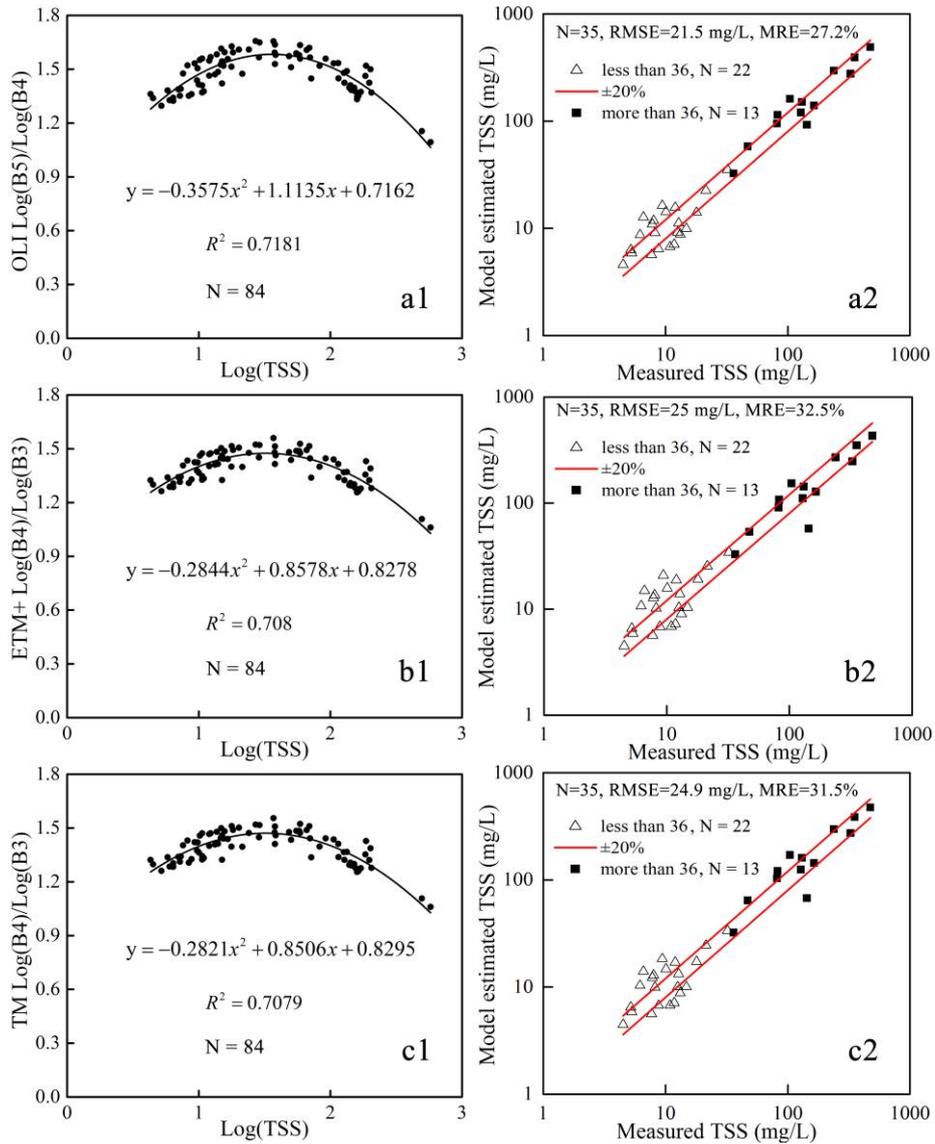
Figure 4. The calibration and validation results of TSS retrieval models: based on 119 in situ data (a) OLI, (b) ETM+ and (c) TM.

5
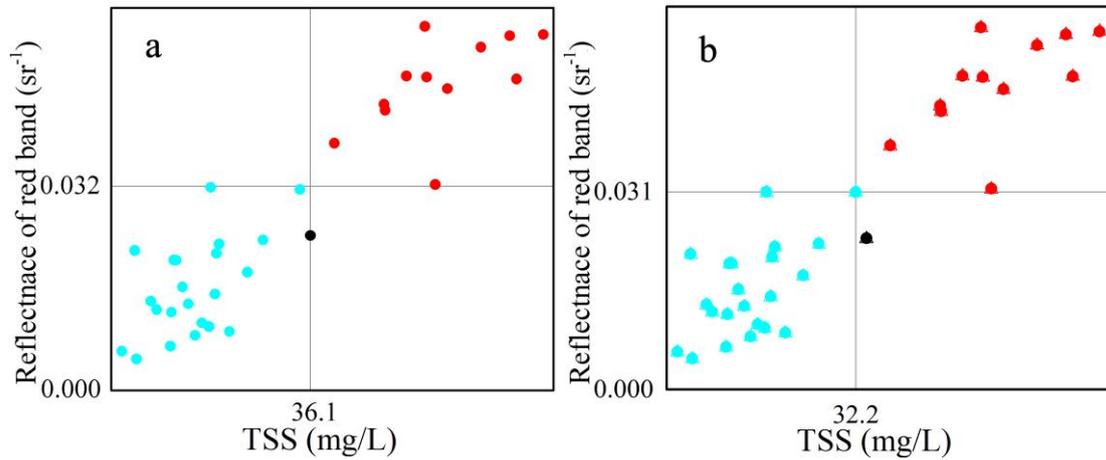
Figure 5. Relationship between the Landsat red band reflectance and corresponding TSS concentration. a: OLI sensor, b: ETM+ and TM sensors.
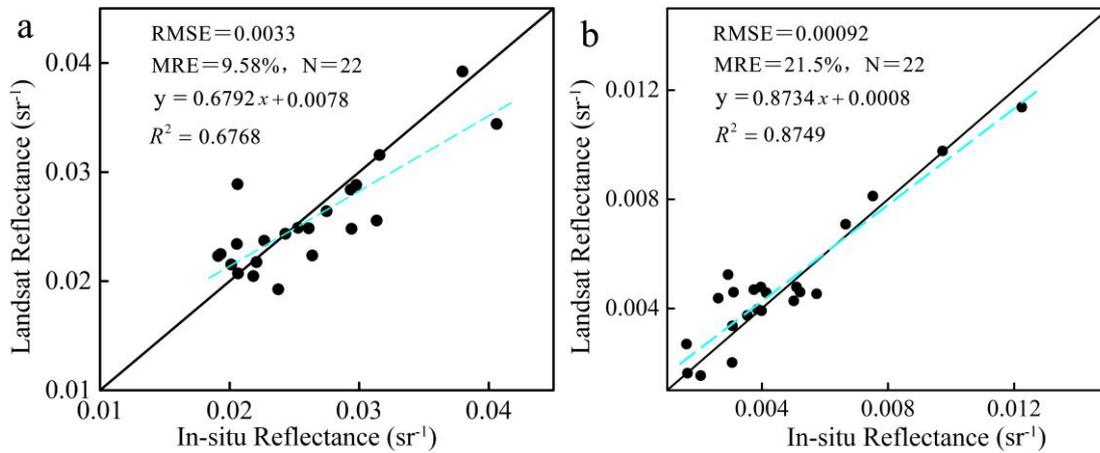

Figure 6. Scatterplot of Landsat measured reflectance versus in-situ reflectance. The former is calculated by averaging over a box of 3x3 pixels centered samples. a: red band, b: near infrared band.
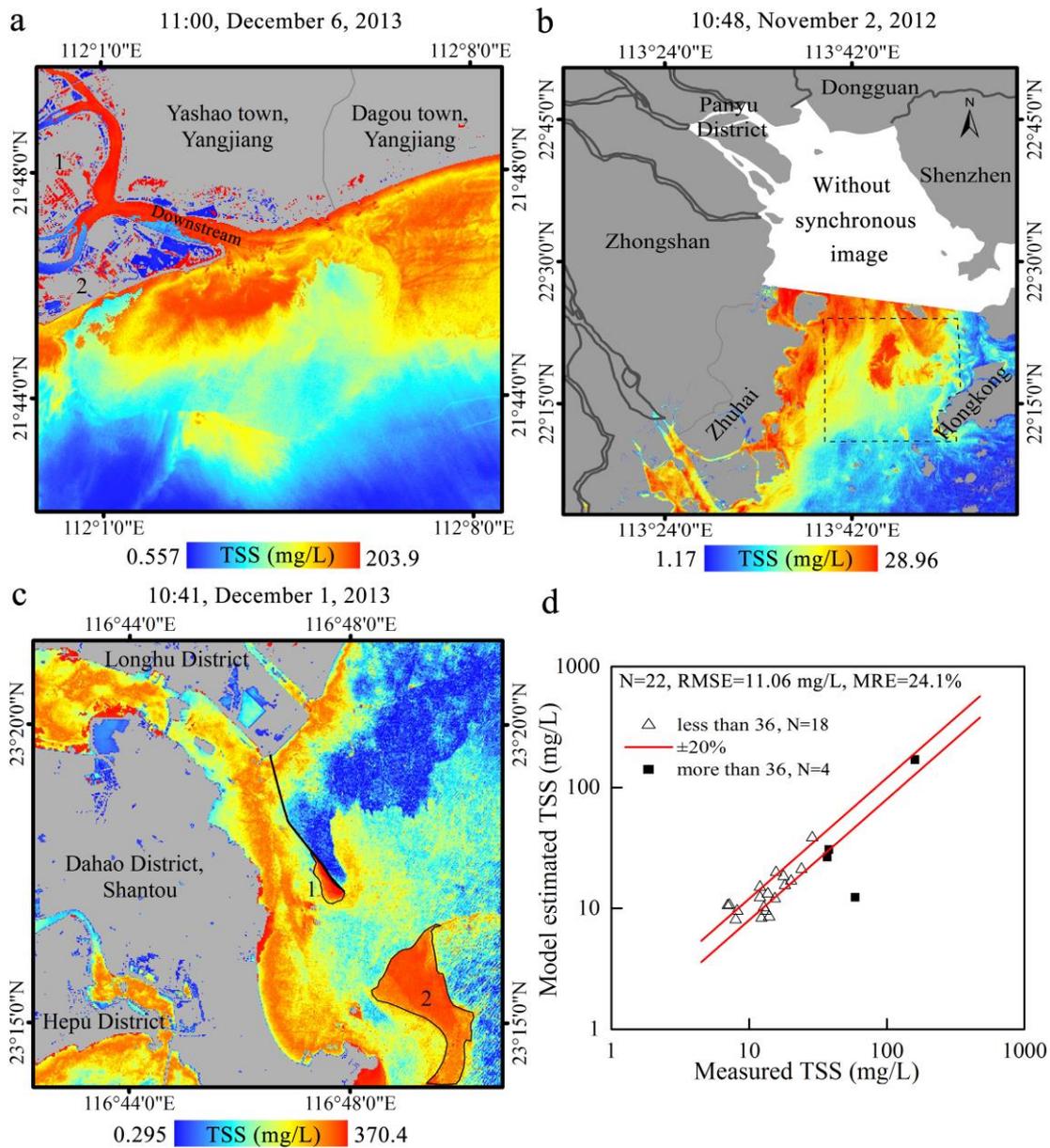
Figure 7. Estimated TSS concentrations based on QRLTSS model in Moyangjiang River Estuary at 11:00 (Beijing time, OLI), on December 6, 2013 (a), Pearl River Estuary at 10:48 (Beijing time, ETM+), on November 2, 2012 (b), Hanjiang River Estuary at 10:41 (Beijing time, OLI), on December 1, 2013 (c), and comparison between the in-situ measured and Landsat imagery inversed TSS concentrations of three estuaries (d). Color scale is the legend of the TSS concentrations, in mg/L.
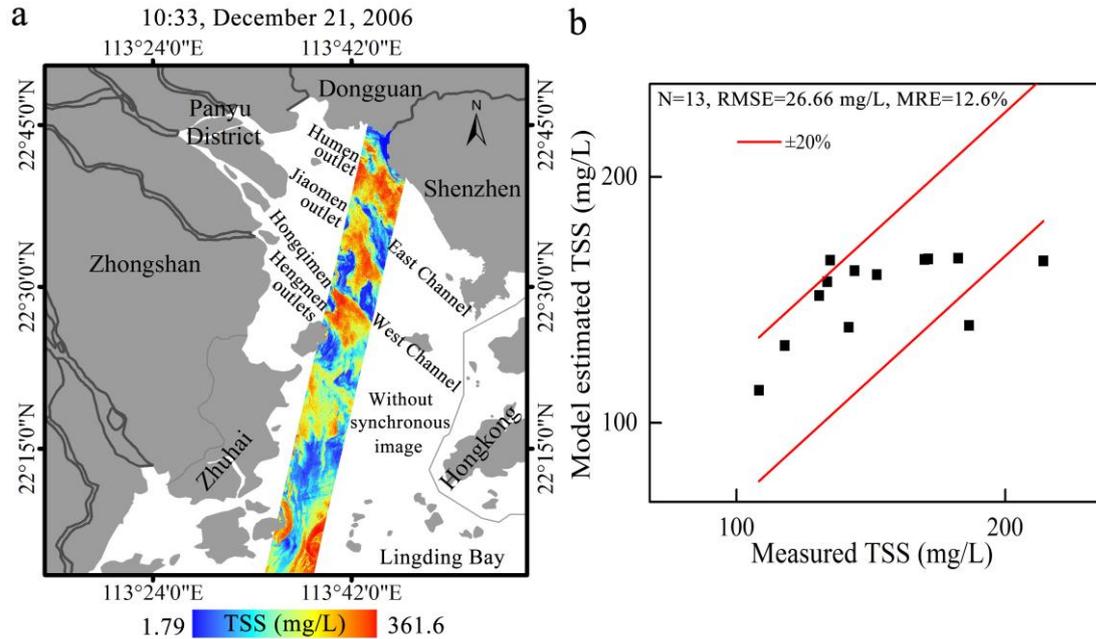
Figure 8. Estimated TSS concentrations based on QRLTSS model from EO-1 Hyperion imagery in Pearl River Estuary at 10:33 (Beijing time), on December 21, 2006 (a) and comparison between the in-situ measured and EO-1 Hyperion imagery inversed TSS concentrations (b). Color scale is the legend of the TSS concentrations, in mg/L.